

LJMU Research Online

Corsi, A, Ho, AYQ, Cenko, SB, Kulkarni, SR, Anand, S, Yang, S, Sollerman, J, Srinivasaragavan, GP, Omand, CMB, Balasubramanian, A, Frail, DA, Fremling, C, Perley, DA, Yao, Y, Dahiwal, AS, De, K, Dugas, A, Hankins, M, Jencson, J, Kasliwal, MM, Tzanidakis, A, Bellm, EC, Laher, RR, Masci, FJ, Purdum, JN and Regnault, N

A Search for Relativistic Ejecta in a Sample of ZTF Broad-lined Type Ic Supernovae

<https://researchonline.ljmu.ac.uk/id/eprint/22171/>

Article

Citation (please note it is advisable to refer to the publisher's version if you intend to cite from this work)

Corsi, A ORCID logo**ORCID: <https://orcid.org/0000-0001-8104-3536>, Ho, AYQ ORCID logo****ORCID: <https://orcid.org/0000-0002-9017-3567>, Cenko, SB ORCID logo****ORCID: <https://orcid.org/0000-0003-1673-970X>, Kulkarni, SR ORCID logo****ORCID: <https://orcid.org/0000-0001-5390-8563>. Anand. S ORCID**

LJMU has developed **LJMU Research Online** for users to access the research output of the University more effectively. Copyright © and Moral Rights for the papers on this site are retained by the individual authors and/or other copyright owners. Users may download and/or print one copy of any article(s) in LJMU Research Online to facilitate their private study or for non-commercial research. You may not engage in further distribution of the material or use it for any profit-making activities or any commercial gain.

The version presented here may differ from the published version or from the version of the record. Please see the repository URL above for details on accessing the published version and note that access may require a subscription.

For more information please contact researchonline@ljmu.ac.uk

<http://researchonline.ljmu.ac.uk/>



A Search for Relativistic Ejecta in a Sample of ZTF Broad-lined Type Ic Supernovae

Alessandra Corsi¹, Anna Y. Q. Ho^{2,3,4,5}, S. Bradley Cenko^{6,7}, Shrinivas R. Kulkarni⁸, Shreya Anand⁸, Sheng Yang^{9,10}, Jesper Sollerman⁹, Gokul P. Srinivasaragavan^{6,7,11}, Conor M. B. Omand⁹, Arvind Balasubramanian¹, Dale A. Frail¹², Christoffer Fremling^{8,13}, Daniel A. Perley¹⁴, Yuhao Yao⁸, Aishwarya S. Dahiwalé¹⁵, Kishalay De¹⁶, Alison Dugas¹⁷, Matthew Hanks¹⁸, Jacob Jencson¹⁹, Mansi M. Kasliwal⁸, Anastasios Tzanidakis²⁰, Eric C. Bellm²¹, Russ R. Laher²², Frank J. Masci²², Josiah N. Purdum⁸, and Nicolas Regnault²³

¹ Department of Physics and Astronomy, Texas Tech University, Box 1051, Lubbock, TX 79409-1051, USA; alessandra.corsi@ttu.edu

² Department of Astronomy, Cornell University, Ithaca, NY 14853, USA

³ Miller Institute for Basic Research in Science, 468 Donner Lab, Berkeley, CA 94720, USA

⁴ Department of Astronomy, University of California, Berkeley, Berkeley, CA 94720, USA

⁵ Lawrence Berkeley National Laboratory, 1 Cyclotron Road, MS 50B-4206, Berkeley, CA 94720, USA

⁶ Astrophysics Science Division, NASA Goddard Space Flight Center, MC 661, Greenbelt, MD 20771, USA

⁷ Joint Space-Science Institute, University of Maryland, College Park, MD 20742, USA

⁸ Division of Physics, Mathematics and Astronomy, California Institute of Technology, Pasadena, CA 91125, USA

⁹ The Oskar Klein Center, Department of Astronomy, Stockholm University, AlbaNova, SE-10691 Stockholm, Sweden

¹⁰ Henan Academy of Sciences, Zhengzhou 450046, Henan, China

¹¹ Department of Astronomy, University of Maryland, College Park, MD 20742, USA

¹² National Radio Astronomy Observatory, Socorro, NM 87801, USA

¹³ Caltech Optical Observatories, California Institute of Technology, Pasadena, CA 91125, USA

¹⁴ Astrophysics Research Institute, Liverpool John Moores University, IC2, Liverpool Science Park, 146 Brownlow Hill, Liverpool L3 5RF, UK

¹⁵ Department of Physics, Michigan Technological University, Fisher Hall 118, 1400 Townsend Drive Houghton, MI 49931, USA

¹⁶ MIT—Kavli Institute for Astrophysics and Space Research, 77 Massachusetts Avenue, Cambridge, MA 02139, USA

¹⁷ Department of Physics and Astronomy, Watanabe 416, 2505 Correa Road, Honolulu, HI 96822, USA

¹⁸ Department of Physics, Arkansas Tech University, 1701 N Boulder Avenue Russellville, AR 72801, USA

¹⁹ Steward Observatory, University of Arizona, 933 North Cherry Avenue, Rm. N204, Tucson, AZ 85721-0065, USA

²⁰ Department of Astronomy, University of Washington, 3910 15th Avenue NE, Seattle, WA 98195, USA

²¹ DIRAC Institute, Department of Astronomy, University of Washington, 3910 15th Avenue NE, Seattle, WA 98195, USA

²² IPAC, California Institute of Technology, 1200 E. California Boulevard, Pasadena, CA 91125, USA

²³ LPNHE, CNRS/IN2P3 & Sorbonne Université, 4 place Jussieu, F-75005 Paris, France

Received 2022 October 16; revised 2023 May 5; accepted 2023 May 8; published 2023 August 16

Abstract

The dividing line between gamma-ray bursts (GRBs) and ordinary stripped-envelope core-collapse supernovae (SNe) is yet to be fully understood. Observationally mapping the variety of ejecta outcomes (ultrarelativistic, mildly relativistic, or nonrelativistic) in SNe of Type Ic with broad lines (Ic-BL) can provide a key test to stellar explosion models. However, this requires large samples of the rare SN Ic-BL events with follow-up observations in the radio, where fast ejecta can be probed largely free of geometry and viewing angle effects. Here, we present the results of a radio (and X-ray) follow-up campaign of 16 SNe Ic-BL detected by the Zwicky Transient Facility (ZTF). Our radio campaign resulted in four counterpart detections and 12 deep upper limits. None of the events in our sample is as relativistic as SN 1998bw and we constrain the fraction of SN 1998bw-like explosions to $<19\%$ (3σ Gaussian equivalent), a factor of ≈ 2 smaller than previously established. We exclude relativistic ejecta with radio luminosity densities in between $\approx 5 \times 10^{27} \text{ erg s}^{-1} \text{ Hz}^{-1}$ and $\approx 10^{29} \text{ erg s}^{-1} \text{ Hz}^{-1}$ at $t \gtrsim 20$ days since explosion for $\approx 60\%$ of the events in our sample. This shows that SNe Ic-BL similar to the GRB-associated SNe 1998bw, 2003lw, and 2010bh, or to the relativistic SNe 2009bb and iPTF17cw, are rare. Our results also exclude an association of the SNe Ic-BL in our sample with largely off-axis GRBs with energies $E \gtrsim 10^{50} \text{ erg}$. The parameter space of SN 2006aj-like events (faint and fast-peaking radio emission) is, on the other hand, left largely unconstrained, and systematically exploring it represents a promising line of future research.

Unified Astronomy Thesaurus concepts: Gamma-ray bursts (629); Core-collapse supernovae (304); Extragalactic radio sources (508)

1. Introduction

Massive stars contribute to the chemical composition of matter as we know it in the universe, and their deaths are accompanied by energetic core-collapse supernovae (SNe) that seed our universe with black holes (BHs) and neutron stars (NSs)—the most exotic objects of the stellar graveyard. Large time-domain surveys of the sky (e.g., York et al. 2000;

Drake et al. 2009; Law et al. 2009; Kaiser et al. 2010; Shappee et al. 2014; Dark Energy Survey Collaboration et al. 2016; Tonry et al. 2018d; Bellm et al. 2019), paired with targeted follow-up efforts, have greatly enriched our view on the final stages of massive star evolution. Yet, a lot remains to be understood about the diverse paths that bring massive stars toward their violent deaths (Langer 2012).

Core-collapse SNe can occur in stars with a hydrogen envelope (Type II) or in stars where hydrogen is almost or completely missing (Type Ib/c, also referred to as stripped-envelope SNe; Filippenko 1997; Matheson et al. 2001; Li et al. 2011; Modjaz et al. 2014; Perley et al. 2020;



Original content from this work may be used under the terms of the [Creative Commons Attribution 4.0 licence](https://creativecommons.org/licenses/by/4.0/). Any further distribution of this work must maintain attribution to the author(s) and the title of the work, journal citation and DOI.

Frohmaier et al. 2021). Type Ib/c SNe constitute approximately 25% of all massive star explosions (Smith et al. 2011), and their pre-SN progenitors are thought to be either massive ($M \gtrsim 20\text{--}25 M_{\odot}$) and metal-rich single stars that have been stripped through stellar mass loss, or the mass donors in close binary systems (at any metallicity) that have initial masses $\gtrsim 8 M_{\odot}$ (e.g., Langer 2012 and references therein).

A small fraction of Type Ib/c SNe show velocities in their optical spectra that are systematically higher than those measured in ordinary SNe Ic at similar epochs. Hence, these explosions are referred to as SNe of Type Ic with broad lines (hereafter, Ic-BL; e.g., Filippenko 1997; Modjaz et al. 2016; Gal-Yam 2017). Compared to Type Ib/c SNe, broad-lined events are found to prefer environments with lower metallicity (in the single star scenario, mass-loss mechanisms also remove angular momentum and are enhanced by higher metallicities), and in galaxies with higher star formation rate densities. Thus, it has been suggested that SN Ic-BL progenitors may be stars younger and more massive than those of normal Type Ic (more massive progenitors can lose their He-rich layers to winds at lower metallicity due to the higher luminosities driving the winds), and/or tight massive binary systems that can form efficiently in dense stellar clusters (e.g., Kelly et al. 2014; Japelj et al. 2018; Modjaz et al. 2020).

The spectroscopic and photometric properties used to classify core-collapse SNe are largely determined by the stars' outer envelopes (envelope mass, radius, and chemical composition; Young 2004). On the other hand, quantities such as explosion energies, nickel masses, and ejecta geometries can be inferred via extensive multiwavelength and multiband observations. These quantities, in turn, can help constrain the properties of the stellar cores (such as mass, density structure, spin, and magnetic fields; see, e.g., Woosley et al. 2002; Burrows et al. 2007; Jerkstrand et al. 2015, and references therein) that are key to determine the nature of the explosion. For example, based on nickel masses and ejecta masses derived from bolometric light curve analyses, Taddia et al. (2019) found that $\gtrsim 21\%$ of Ic-BL progenitors are compatible with massive ($\gtrsim 28 M_{\odot}$), possibly single stars, whereas $\gtrsim 64\%$ could be associated with less massive stars in close binary systems.

Understanding the progenitor scenario of SNe Ic-BL is particularly important as these SNe challenge greatly the standard explosion mechanism of massive stars (e.g., Mezzacappa et al. 1998; MacFadyen & Woosley 1999; Heger et al. 2003; Woosley & Heger 2006; Janka et al. 2007; Janka 2012; Smith 2014; Foglizzo et al. 2015; Müller 2020; Schneider et al. 2021, and references therein). The energies inferred from optical spectroscopic modeling of Ic-BL events are of order $\approx 10^{52}$ erg, in excess of the $\approx 10^{51}$ erg inferred in typical SNe Ib/c, while ejecta masses are comparable or somewhat higher (Taddia et al. 2019). In the traditional core-collapse scenario, neutrino irradiation from the proto-NS revives the core-bounce shock, making the star explode. However, the neutrino mechanism cannot explain the more energetic SNe Ic-BL. Unveiling the nature of an engine powerful enough to account for the extreme energetics of SNe Ic-BL is key to understanding the physics behind massive stellar deaths, and remains as of today an open question.

A compelling scenario invokes the existence of a jet or a newly born magnetar as the extra source of energy needed to explain SNe Ic-BL (e.g., Burrows et al. 2007; Papish & Soker 2011; Lazzati et al. 2012; Gilkis & Soker 2014;

Mazzali et al. 2014; Gilkis et al. 2016; Soker & Gilkis 2017; Barnes et al. 2018; Shankar et al. 2021). The rapid rotation of a millisecond proto-NS formed in the collapse of a rotating massive star can amplify the NS magnetic field to $\gtrsim 10^{15}$ G, creating a magnetar. The magnetar spins down quickly via magnetic braking, and in some cases magneto-rotational instabilities can launch a collimated jet that drills through the outer layers of the star producing a gamma-ray burst (GRB; e.g., Heger et al. 2003; Izzard et al. 2004; Woosley & Heger 2006; Burrows et al. 2007; Bugli et al. 2020, 2021). These jets can transfer sufficient energy to the surrounding stellar material to explode it as an SN.

The above scenario is particularly interesting in light of the fact that SNe Ic-BL are also the only type of core-collapse events that, observationally, have been unambiguously linked to GRBs (e.g., Woosley & Bloom 2006; Cano et al. 2017, and references therein). GRBs are characterized by bright afterglows that emit radiation from radio to X-rays, and are unique laboratories for studying relativistic particle acceleration and magnetic field amplification processes (Piran 2004; Mészáros 2006). In between ordinary SNe Ic-BL and cosmological GRBs is a variety of transients that we still have to characterize fully. Among those are low-luminosity GRBs, of which the most famous example is GRB 980425, associated with the radio-bright Type Ic-BL SN 1998bw (Galama et al. 1998; Kulkarni et al. 1998).

Recently, Shankar et al. (2021) used the jetted outflow model produced from a consistently formed protomagnetar in a 3D core-collapse SN to extract a range of central engine parameters (energy E_{eng} and opening angle θ_{eng}) that were then used as input to hydrodynamic models of jet-driven explosions. The output of these models, in turn, were used to derive predicted SN light curves and spectra from different viewing angles, and found to be in agreement with SN Ic-BL optical observables (see also Barnes et al. 2018). It was also shown that additional energy from the engine can escape through the tunnel drilled in the star as an ultrarelativistic jet (GRB) with energy $\approx 10^{51}$ erg. On the other hand, an SN Ic-BL can be triggered even if the jet engine fails to produce a successful GRB jet. The duration of the central engine, t_{eng} , together with E_{eng} and θ_{eng} , are critical to determining the fate of the jet (Lazzati et al. 2012).

A more general scenario where the high-velocity ejecta found in SNe Ic-BL originate from a cocoon driven by a relativistic jet (regardless of the nature of the central engine) is also receiving attention. In this scenario, cosmological long GRBs are explosions where the relativistic jet breaks out successfully from the stellar envelope, while low-luminosity GRBs and SNe Ic-BL that are not associated with GRBs represent cases where the jet is choked (see, e.g., Piran et al. 2019; Eisenberg et al. 2022; Gottlieb et al. 2022; Pais et al. 2023, and references therein).

Overall, the dividing line between successful GRB jets and failed ones is yet to be fully explored observationally, and observed jet outcomes in SNe Ic-BL have not yet been systematically compared to model outputs. While we know that SNe discovered by means of a GRB are all of Type Ic-BL, the question that remains open is whether all SNe Ic-BL make a GRB (jet), at least from some viewing angle, or if instead jet-powered SNe Ic-BL are intrinsically different and rarer than ordinary SNe Ic-BL. Indeed, due to the collimation of GRB jets, it is challenging to understand whether all SNe Ic-BL are linked to successful GRBs: a nondetection in γ - or X-rays

could simply be due to the explosion being directed away from us. Radio follow-up observations are needed to probe the explosions' fastest-moving ejecta ($\gtrsim 0.2c$) largely free of geometry and viewing angle constraints. Determining observationally what is the fraction of Type Ic-BL explosions that output jets which successfully break out of the star (as mildly relativistic or ultrarelativistic ejecta), and measuring their kinetic energies via radio calorimetry, can provide jet-engine explosion models a direct test of their predictions.

Using one of the largest sample of SNe Ic-BL with deep radio follow-up observations (which included 15 SNe Ic-BL discovered by the Palomar Transient Factory, PTF/iPTF; Law et al. 2009), Corsi et al. (2016) already established that $<41\%$ of SNe Ic-BL harbor relativistic ejecta similar to that of SN 1998bw. Here, we present the results of a systematic radio follow-up campaign of an additional 16 SNe Ic-BL (at $z \lesssim 0.05$) detected independently of γ -rays by the Zwicky Transient Facility (ZTF; Bellm et al. 2019; Graham et al. 2019). This study greatly expands our previous works on the subject (Corsi et al. 2014, 2016, 2017). Before the advent of PTF and ZTF, the comparison between jet-engine model outcomes and radio observables was severely limited by the rarity of SN Ic-BL discoveries (e.g., Berger et al. 2003; Soderberg et al. 2006a) and/or by selection effects (e.g., Woosley & Bloom 2006)—out of the thousands of jets identified, nearly all were discovered at large distances via their high-energy emission (implying aligned jet geometry and ultrarelativistic speeds). In this work, we aim to provide a study free of these biases.

Our paper is organized as follows. In Section 2 we describe our multiwavelength observations; in the Appendix we describe in more details the SNe Ic-BL included in our sample. In Section 3 we model the optical, X-ray, and radio properties of the SNe presented here and derive constraints on their progenitor and ejecta properties. Finally, in Section 4 we summarize and conclude. Hereafter we assume cosmological parameters of $H_0 = 69.6 \text{ km s}^{-1} \text{ Mpc}^{-1}$, $\Omega_M = 0.286$, $\Omega_{\text{vac}} = 0.714$ (Bennett et al. 2014). All times are given in UT unless otherwise stated.

2. Multiwavelength Observations

We have collected a sample of 16 SNe Ic-BL observed with the ZTF and with follow-up observations in the radio. The SNe Ic-BL included in our sample are listed in Table 1. We selected these SNe largely based on the opportunistic availability of follow-up observing time on the Karl G. Jansky Very Large Array (VLA). For the majority of the Ic-BL SNe in our sample, our VLA trigger criterion was simply the spectral classification of the SN as a Ic-BL. For a small number (four out of 16) of the SNe in our sample, VLA observations were triggered via Swift Guest Investigator programs led by our team (see the last column in Table 2). In this last case, a luminosity distance within 150–200 Mpc was also required as a trigger criterion. The sample of SNe presented here doubles the sample of SNe Ic-BL with deep VLA observations presented in Corsi et al. (2016).

The SNe considered in this work are generally closer than the PTF/iPTF sample of SNe Ic-BL presented in Taddia et al. (2019). In fact, their median redshift (≈ 0.037) is about twice as small as the median redshift of the PTF/iPTF SN Ic-BL sample (≈ 0.076 ; Taddia et al. 2019). However, the median redshift of the ZTF SNe in our sample is compatible with the median

Table 1
The Sample of 16 SNe Ic-BL Analyzed in This Work

SN (ZTF Name)	R.A., Decl. (J2000) (hh:mm:ss dd:mm:ss)	z	d_L (Mpc)
2018etk (18abklarx)	15:17:02.53 +03:56:38.7	0.044	196
2018hom (18acbwxc)	22:59:22.96 +08:45:04.6	0.030	132
2018hxo (18acaimrb)	21:09:05.80 +14:32:27.8	0.048	214
2018jex (18acpeekw)	11:54:13.87 +20:44:02.4	0.094	434
2019hsx (19aawqcg)	18:12:56.22 +68:21:45.2	0.021	92
2019xcc (19adaiomg)	11:01:12.39 +16:43:29.1	0.029	128
2020jqm (20aazkjfv)	13:49:18.57 −03:46:10.4	0.037	164
2020lao (20abbbplei)	17:06:54.61 +30:16:17.3	0.031	137
2020rph (20abswdbg)	03:15:17.83 +37:00:50.8	0.042	187
2020tkx (20abzoeiw)	18:40:09.01 +34:06:59.5	0.027	119
2021xv (21aadatfg)	16:07:32.82 +36:46:46.2	0.041	182
2021aug (21aafnunh)	01:14:04.81 +19:25:04.7	0.041	182
2021epp (21aaoerlm)	08:10:55.27 −06:02:49.3	0.038	168
2021htb (21aardvol)	07:45:31.19 +46:40:01.3	0.035	155
2021hyz (21aartgiv)	09:27:36.51 +04:27:11.0	0.046	205
2021ywf (21acbnfos)	05:14:10.99 +01:52:52.4	0.028	123

Note. For each SN we provide the IAU name, the ZTF name, the position, redshift, and luminosity distance.

redshift (≈ 0.042) of the full ZTF SN Ic-BL population presented in G. P. Srinivasaragavan et al. (2023, in preparation). A subset of the SNe Ic-BL presented here is also analyzed in a separate paper and in a different context (r-process nucleosynthesis; Anand et al. 2023). In this work, we report for the first time the results of our radio follow-up campaign of these events. We note that the Asteroid Terrestrial-impact Last Alert System (ATLAS; Tonry et al. 2018d) has contributed to several of the SN detections considered here (see the Appendix). Three of the SNe Ic-BL in our sample were also reported in the recently released bright SN catalog by the All-Sky Automated Survey for Supernovae (ASAS-SN; Neumann et al. 2023).

In what follows, we describe the observations we carried for this work. In the Appendix we give more details on each of the SNe Ic-BL in our sample.

2.1. ZTF Photometry

All photometric observations presented in this work were conducted with the Palomar Schmidt 48-inch (P48) Samuel Oschin telescope as part of the ZTF survey (Bellm et al. 2019; Graham et al. 2019), using the ZTF camera (Dekany et al. 2020). In default observing mode, ZTF uses 30 s exposures, and survey observations are carried out in r and g band, down to a typical limiting magnitude of ≈ 20.5 mag. P48 light curves were derived using the ZTF pipeline (Masci et al. 2019) and forced photometry (see Yao et al. 2019). Hereafter, all reported magnitudes are in the AB system. The P48 light curves are shown in Figures 1 and 2. All the light curves presented in this work will be made public on the Weizmann Interactive Supernova Data Repository²⁴ (WiSeREP; Yaron & Gal-Yam 2012).

2.2. Optical Spectroscopy

Preliminary spectral type classifications of several of the SNe in our sample were obtained with the Spectral Energy

²⁴ <https://www.wiserep.org/>

Table 2
VLA Follow-up Observations of the 16 SNe Ic-BL in Our Sample

SN	T_{VLA}^a (MJD)	ν (GHz)	F_ν (μ Jy)	Conf.	Nom. Syn. (FWHM; arcseconds)	Project
2018etk	58363.08	6.3	90.1 ± 8.7^b	D	12	VLA/18A-176 ^d
	58374.09	14	41 ± 11	D	4.6	VLA/18A-176 ^d
	58375.03	6.3	89.7 ± 8.8^b	D	12	VLA/18A-176 ^d
	59362.27	6.2	78.5 ± 6.3^b	D	12	VLA/20B-149 ^d
2018hom	58428.04	6.6	133 ± 11	D	12	VLA/18A-176 ^d
2018hxo	58484.73	6.4	$\lesssim 234^c$	C	3.5	VLA/18A-176 ^d
2018jex	58479.38	6.4	$\lesssim 28$	C	3.5	VLA/18A-176 ^d
2019hsx	58671.14	6.2	$\lesssim 19$	BnA	1.0	VLA/19B-230 ^d
2019xcc	58841.43	6.3	62.7 ± 8.7^b	D	12	VLA/19B-230 ^d
	58876.28	6.3	60.1 ± 8.5^b	D	12	VLA/19B-230 ^d
	59363.00	6.3	50.4 ± 8.1^b	D	12	VLA/20B-149 ^d
2020jqm	58997.03	5.6	175 ± 13	C	3.5	SG0117 ^d
	59004.03	5.6	310 ± 19	C	3.5	SG0117 ^d
	59028.48	5.5	223 ± 18	B	1.0	VLA/20A-568 ^d
	59042.95	5.7	202 ± 15	B	1.0	VLA/20A-568 ^d
	59066.09	5.5	136 ± 13	B	1.0	VLA/20A-568 ^d
	59088.03	5.5	168 ± 13	B	1.0	VLA/20A-568 ^d
	59114.74	5.5	620 ± 33	B	1.0	VLA/20A-568 ^d
	59240.37	5.5	720 ± 37	A	0.33	VLA/20B-149 ^d
2020lao	59006.21	5.2	$\lesssim 33$	C	3.5	SG0117 ^d
	59138.83	5.5	$\lesssim 21$	B	1.0	SG0117 ^d
2020rph	59089.59	5.5	42.7 ± 7.4	B	1.0	SG0117 ^d
	59201.28	5.5	43.9 ± 7.0	A	0.33	SG0117 ^d
2020tkx	59117.89	10	272 ± 16	B	0.6	VLA/20A-374 ^e
	59136.11	10	564 ± 29	B	0.6	VLA/20A-374 ^e
	59206.92	5.5	86.6 ± 7.3	A	0.33	VLA/20B-149 ^d
2021xv	59242.42	5.5	$\lesssim 23$	A	0.33	VLA/20B-149 ^d
	59303.24	5.2	$\lesssim 29$	D	12	VLA/20B-149 ^d
	59353.11	5.2	34.3 ± 8.1^b	D	12	VLA/20B-149 ^d
2021aug	59254.75	5.2	$\lesssim 22$	A	0.33	VLA/20B-149 ^d
	59303.62	5.4	$\lesssim 45$	D	12	VLA/20B-149 ^d
	59353.48	5.4	$\lesssim 30$	D	12	VLA/20B-149 ^d
2021epp	59297.06	5.3	$(2.62 \pm 0.13) \times 10^{3b}$	D	12	VLA/20B-149 ^d
	59302.99	5.1	$(2.82 \pm 0.18) \times 10^{3b}$	D	12	VLA/20B-149 ^d
	59352.83	5.3	$(2.75 \pm 0.20) \times 10^{3b}$	D	12	VLA/20B-149 ^d
2021htb	59324.94	5.2	50 ± 10^b	D	12	VLA/20B-149 ^d
	59352.87	5.2	59.4 ± 9.5^b	D	12	VLA/20B-149 ^d
2021hyz	59326.08	5.2	38 ± 11	D	12	VLA/20B-149 ^d
	59352.99	5.5	$\lesssim 30$	D	12	VLA/20B-149 ^d
2021ywf	59487.57	5.0	83 ± 10	B	1.0	SH0105 ^d
	59646.12	5.4	19.8 ± 6.3	A	0.33	SH0105 ^a

Note. For all of the observations of the SNe in our sample we report the mid MJD of the VLA observation; the central observing frequency; the measured flux density (all flux density upper limits are calculated at 3σ unless otherwise noted); the VLA array configuration; the FWHM of the VLA nominal synthesized beam; and the VLA project code under which the observations were conducted. See Sections 2.4 and 3.5 for discussion.

^a Mid MJD time of the VLA observation (total time including calibration).

^b Resolved or marginally resolved with emission likely dominated by the host galaxy.

^c Image is dynamic range limited due to the presence of a bright source in the field.

^d PI: Corsi.

^e PI: Ho.

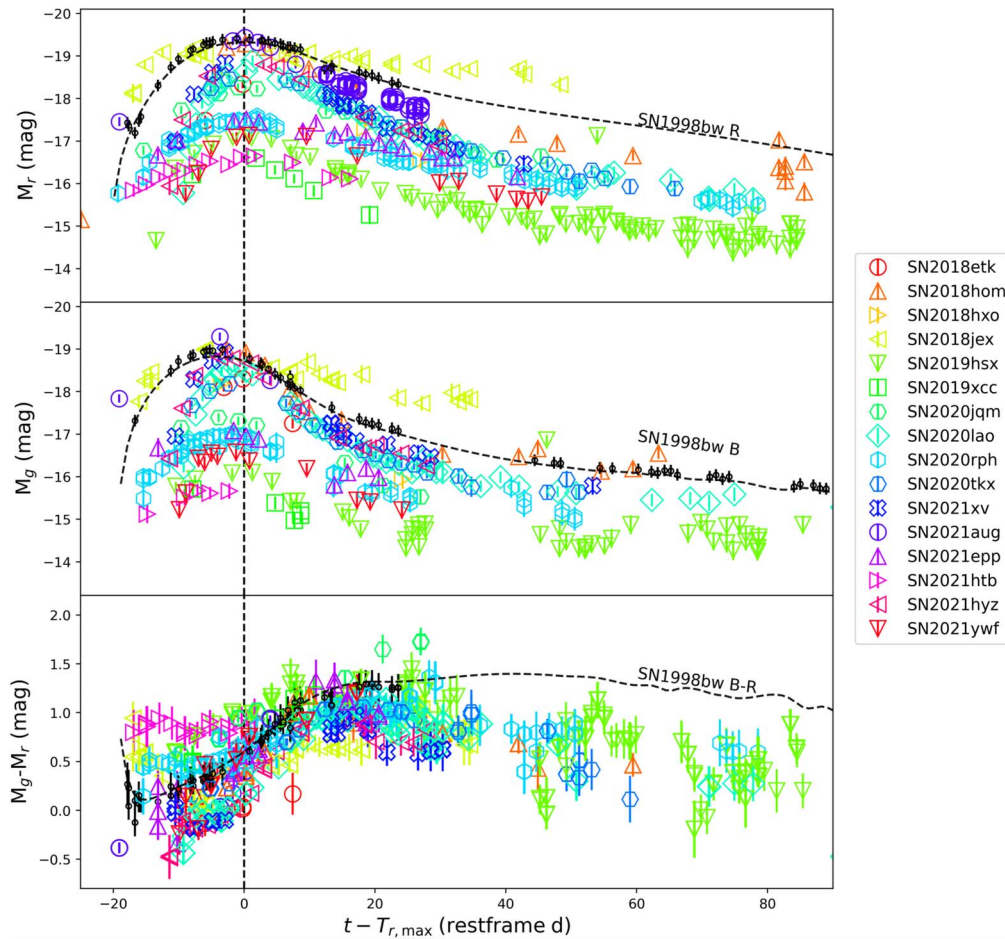


Figure 1. P48 r - (top) and g -band (middle) light curves for the SNe Ic-BL in our sample, compared with the R - and B -band light curves of SN 1998bw, respectively. The bottom panel shows the corresponding color evolution. Observed AB magnitudes are corrected for Milky Way (MW) extinction. The archetypal SN 1998bw is shown in black solid points, and its Gaussian process interpolation in black dashed lines. See also Anand et al. (2023) and G. P. Srinivasaragavan et al. (2023, in preparation).

Distribution Machine (SEDM) mounted on the Palomar 60-inch telescope (P60), and quickly reported to the Transient Name Server (TNS). SEDM is a very-low-resolution ($R \sim 100$) integral field unit spectrograph optimized for transient classification with high observing efficiency (Blagorodnova et al. 2018; Rigault et al. 2019).

After initial classification, typically further spectroscopic observations are carried out as part of the ZTF transient follow-up programs to confirm and/or improve classification, and to characterize the time-evolving spectral properties of interesting events. Among the series of spectra obtained for each of the SNe presented in this work, we select one good quality photospheric phase spectrum (Figures 3 and 4; gray) on which we run SNID (Blondin & Tonry 2007) to obtain the best match to an SN Ic-BL template (black), after clipping the host emission lines and fixing the redshift to that derived either from the Sloan Digital Sky Survey (SDSS) host galaxy or from spectral line fitting ($H\alpha$; see the Appendix for further details). Hence, in addition to SEDM, in this work we also made use of the following instruments: the Double Spectrograph (DBSP; Oke et al. 1995), a low-to-medium-resolution grating instrument for the Palomar 200-inch telescope Cassegrain focus that uses a dichroic to split light into separate red and blue channels observed simultaneously; the Low Resolution Imaging Spectrometer (LRIS; Oke & Gunn 1982; Oke et al. 1995), a visible-wavelength imaging and spectroscopy

instrument operating at the Cassegrain focus of Keck I; and the Alhambra Faint Object Spectrograph and Camera (ALFOSC), a CCD camera and spectrograph installed at the Nordic Optical Telescope (NOT; Djupvik & Andersen 2010). All spectra presented in this work will be made public on WISEREP.

2.3. X-Ray Follow up with Swift

For eight of the 16 SNe presented in this work we carried out follow-up observations in X-rays using the X-Ray Telescope (XRT; Burrows et al. 2005) on the Neil Gehrels Swift Observatory (Gehrels et al. 2004). We selected these SNe based on a combination of opportunistic availability of observing time via Swift Guest Investigator programs led by our team (for SNe 2020jqm, 2020lao, 2020rph, and 2021ywf; see also column 7 in Table 3), and the relevance of some events for specific ZTF experiments, such as the census of the local universe and the redshift completeness fraction ones (for SNe 2018etk, 2018hom, and 2019hsx; see also Graham et al. 2019). For SN 2021hyz, Swift observations were carried out serendipitously via an independent program (PI: Paolo Giommi).

We analyzed these observations using the online XRT tools,²⁵ as described in Evans et al. (2009). We correct for

²⁵ See https://www.swift.ac.uk/user_objects/

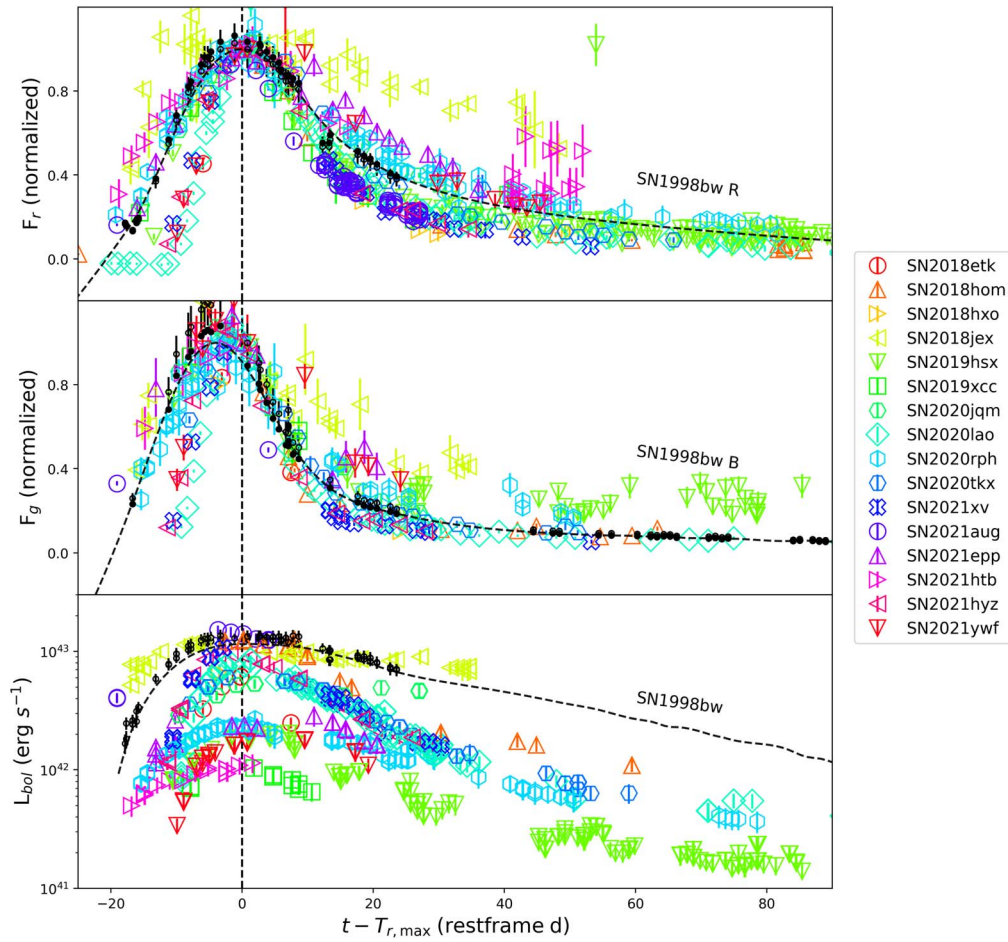


Figure 2. Top and middle panels: same as Figure 1 but in flux space and with fluxes normalized to their Gaussian process maximum. Bottom panel: bolometric light curves. We converted $g - r$ to bolometric magnitudes with the empirical relations of Lyman et al. (2014, 2016). See also Anand et al. (2023) and G. P. Srinivasaragavan et al. (2023, in preparation).

Galactic absorption, and adopt a power-law spectrum with photon index $\Gamma=2$ for count rate to flux conversion for nondetections, and for detections (two out of nine events) where the number of photons collected is too small to enable a meaningful spectral fit (one out of two detections). Table 4 presents the results from coadding all observations of each source.

2.4. Radio Follow up with the VLA

We observed the fields of the SNe Ic-BL in our sample with the VLA via several of our programs using various array configurations and receiver settings (Table 2).

The VLA raw data were calibrated in CASA (McMullin et al. 2007) using the automated VLA calibration pipeline. After manual inspection for further flagging, the calibrated data were imaged using the `tclean` task. Peak fluxes were measured from the cleaned images using `imstat` and circular regions centered on the optical positions of the SNe, with radius equal to the nominal width (FWHM) of the VLA synthesized beam (see Table 2). The rms noise values were estimated with `imstat` from the residual images. Errors on the measured peak flux densities in Table 2 are calculated adding a 5% error in quadrature to the measured rms values. This accounts for systematic uncertainties on the absolute flux calibration.

We checked all of our detections (peak flux density above 3σ) for the source morphology (extended versus point-like),

and ratio between the integrated and peak fluxes using the CASA task `imfit`. All sources for which these checks provided evidence for extended or marginally resolved emission are marked accordingly in Table 2. For nondetections, upper limits on the radio flux densities are given at the 3σ level unless otherwise noted.

3. Multiwavelength Analysis

3.1. Photospheric Velocities

We confirm the SN Type Ic-BL classification of each object in our sample by measuring the photospheric velocities (v_{ph}). SNe Ic-BL are characterized by high expansion velocities evident in the broadness of their spectral lines. A good proxy for the photospheric velocity is that derived from the maximum absorption position of Fe II $\lambda 5169$ (e.g., Modjaz et al. 2016). We caution, however, that estimating this velocity is not easy given the strong line blending. We first preprocessed one high-quality spectrum per object using the IDL routine `WOMBAT`, then smoothed the spectrum using the IDL routine `SNspecFFTsmooth` (Liu et al. 2016), and finally ran `SESNSpectraLib` (Liu et al. 2016; Modjaz et al. 2016) to obtain final velocity estimates.

In Figure 5 we show a comparison of the photospheric velocities estimated for the SNe in our sample with those derived from spectroscopic modeling for a number of

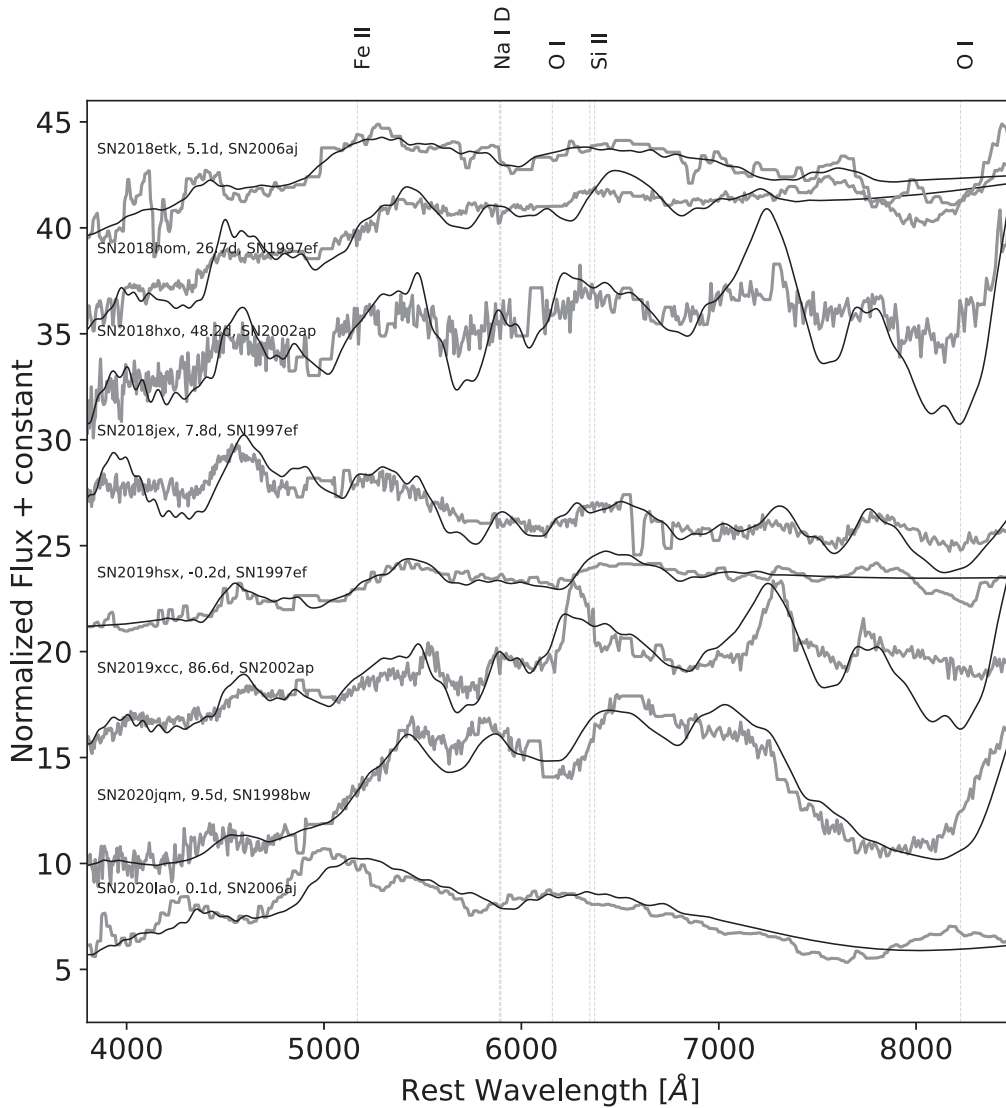


Figure 3. Photospheric phase spectra (gray) plotted along with their SNID best-match templates (black) for the first half of the SNe Ic-BL in our sample. Spectra are labeled with their IAU name and spectroscopic phase (since r -band maximum; see Table 5). We note that the spectra used to estimate the photospheric velocities of SN 2019xcc, SN 2020lao, and SN 2020jqm presented in Table 5 are different from the ones shown here for classification purposes. This is because for spectral classification we prefer later-time but higher-resolution spectra, while for velocity measurements we prefer earlier-time spectra even if taken with the lower-resolution SEDM. All spectra presented in this work will be made public on WISEREP.

SNe Ib/c. The velocities measured for our sample are compatible, within the measurement errors, with what was observed for the PTF/iPTF samples. Measured values for the photospheric velocities with the corresponding rest-frame phase in days since maximum r -band light of the spectra that were used to measure them are also reported in Table 5.

We note that the spectra used to estimate the photospheric velocities of SN 2019xcc, SN 2020lao, and SN 2020jqm are different from those used for the classifications of those events as SNe Ic-BL (see the Appendix and Figure 3). This is because for spectral classification we prefer later-time but higher-resolution spectra, while for velocity measurements we prefer earlier-time spectra even if taken with the lower-resolution SEDM.

3.2. Bolometric Light Curve Analysis

In our analysis we correct all ZTF photometry for Galactic extinction, using the MW color excess $E(B - V)_{\text{MW}}$ toward the positions of the SNe. These are all obtained from

Schlafly & Finkbeiner (2011). All reddening corrections are applied using the Cardelli et al. 1989 extinction law with $R_V = 3.1$. After correcting for MW extinction, we interpolate our P48 forced-photometry light curves using a Gaussian process via the GEORGE²⁶ package with a stationary Matern32 kernel and the analytic functions of Bazin et al. (2009) as the mean for the flux form. As shown in Figure 1, the color evolution of the SNe in our sample are not too dissimilar with one another, which implies that the amount of additional host extinction is small. Hence, we set the host extinction to zero. Next, we derive bolometric light curves calculating bolometric corrections from the g - and r -band data following the empirical relations of Lyman et al. (2014, 2016). For SN 2018hxo, since there is only one g -band detection, we assume a constant bolometric correction to estimate its bolometric light curve. These bolometric light curves are shown in the bottom panel of Figure 2.

²⁶ <https://george.readthedocs.io>

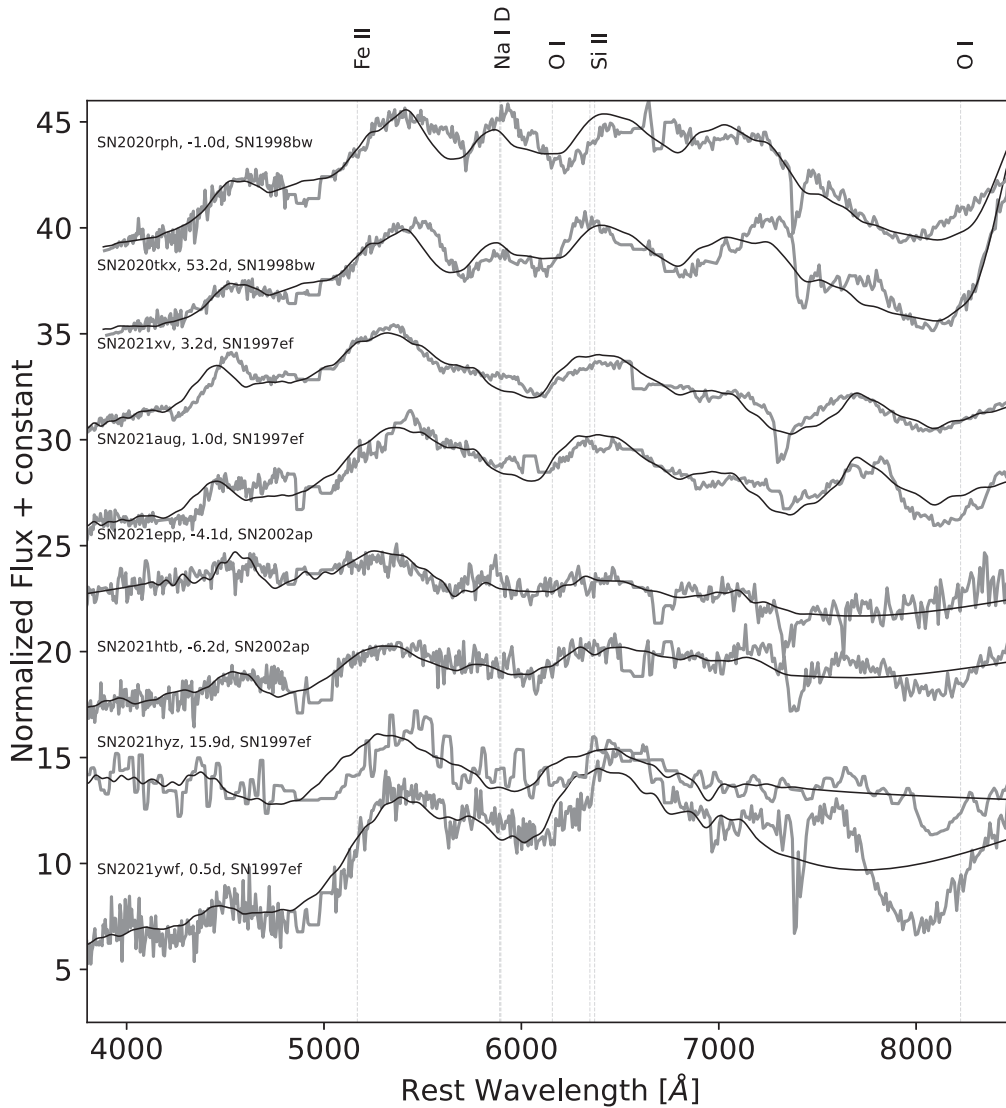


Figure 4. Same as Figure 3 but for the second half of the SNe Ic-BL in our sample. All spectra presented in this work will be made public on WISEREP.

We estimate the explosion times T_{exp} of the SNe in our sample as follows. For SN 2021aug, we fit the early ZTF light curve data following the method presented in Miller et al. (2020), where we fix the power-law index of the rising early-time temporal evolution to $\alpha = 2$, and derive an estimate of the explosion time from the fit. For most of the other SNe in our sample, the ZTF r - and g -band light curves lack enough early-time data to determine an estimate of the explosion time following the formulation of Miller et al. (2020). For all these SNe we instead set the explosion time to the midpoint between the last nondetection prior to discovery, and the first detection. Results on T_{exp} are reported in Table 5.

We fit the bolometric light curves around peak (-20 to 60 rest-frame days relative to peak) to a model using the Arnett formalism (Arnett 1982), with the nickel mass (M_{Ni}) and characteristic timescale τ_m as free parameters (see, e.g., Equation A1 in Valenti et al. 2008). The derived values of M_{Ni} (Table 5) have a median of $\approx 0.22 M_{\odot}$, compatible with the median value found for SNe Ic-BL in the PTF sample by Taddia et al. (2019), somewhat lower than for SN 1998bw for which the estimated nickel mass values are in the range $(0.4\text{--}0.7) M_{\odot}$, but comparable to the $M_{\text{Ni}} \approx 0.19\text{--}0.25 M_{\odot}$

estimated for SN 2009bb (see, e.g., Lyman et al. 2016; Afsariardchi et al. 2021). We note that events such as SN 2019xcc and SN 2021htb have relatively low values of M_{Ni} , which are however compatible with the range of $0.02\text{--}0.05 M_{\odot}$ expected for the nickel mass of magnetar-powered SNe Ic-BL (Nishimura et al. 2015; Suwa & Tominaga 2015; Chen et al. 2017). We also note that the median value of M_{Ni} derived for the sample of Ic-BL SNe presented here is compatible with the median value of $\approx 0.23 M_{\odot}$ we find for the larger sample of ZTF Ic-BL presented in G. P. Srinivasaragavan et al. (2023, in preparation).

Next, from the measured characteristic timescale τ_m of the bolometric light curve, and the photospheric velocities estimated via spectral fitting (see the previous section) we derive the ejecta mass (M_{ej}) and the kinetic energy (E_k) via the following relations (see, e.g., Equations (1) and (2) in Lyman et al. 2016):

$$\tau_m^2 v_{\text{ph,max}} = \frac{2\kappa}{13.8c} M_{\text{ej}}, \quad v_{\text{ph,max}}^2 = \frac{5}{3} \frac{2E_k}{M_{\text{ej}}}, \quad (1)$$

where we assume a constant opacity of $\kappa = 0.07 \text{ g cm}^{-2}$.

Table 3
Properties of the Radio Ejecta of the SNe in Our Sample for Which We Detect a Radio Counterpart

SN	β_s	\dot{M} ($M_\odot \text{ yr}^{-1}$)	E_r (erg)	E_r/E_k
2018hom	0.35	1.1×10^{-6}	3.6×10^{47}	$<0.04\%$
2020jqm	0.33(0.048)	$3.0 \times 10^{-6}(2.7 \times 10^{-4})$	$2.0(5.7) \times 10^{48}$	0.04%(0.1%)
2020tkx	0.14	1.7×10^{-5}	1.1×10^{48}	$<0.07\%$
2021ywf	0.19	2.2×10^{-6}	2.3×10^{47}	0.02%

Note. We report the SN name, the estimated SN shock speed normalized to the speed of light (β_s), the mass-loss rate of the pre-SN progenitor (\dot{M}), the energy coupled to the fastest (radio-emitting) ejecta (E_r), and the ratio between the last and the kinetic energy of the explosion (estimated from the optical light curve modeling, E_k). See Section 3.5 for a discussion of these estimates and their uncertainties.

Table 4
Swift/XRT Observations of Nine of the 16 SNe Ic-BL in Our Sample

SN	T_{XRT} (MJD)	$T_{\text{XRT}} - T_{\text{exp}}$ (d)	Exp. (ks)	$F_{0.3-10 \text{ keV}}$ ($10^{-14} \text{ erg cm}^{-2} \text{ s}^{-1}$)
2018etk	58377.85	49 ± 1	4.8	<4.2
2018hom	58426.02	$9.0^{+0.4}_{-0.7}$	4.3	<6.4
2019hsx	58684.15	$53^{+0.5}_{-0.4}$	15	$6.2^{+2.3}_{-1.8}$
2020jqm	59002.09	23 ± 1	7.4	<3.3
2020lao	59007.40	14 ± 1	14	<2.9
2020rph	59088.89	16.43 ± 0.02	7.5	<3.6
2020tkx	59125.38	22 ± 4	8.1	<3.3
2021hyz	59373.09	66.9 ± 0.9	4.7	<3.5
2021ywf	59487.60	19.7 ± 0.5	7.2	$5.3^{+4.9}_{-3.3}$

Note. We provide the MJD of the Swift observations, the epoch of the XRT observations since the estimated explosion time (Table 4) in the observer's frame, the XRT exposure time, and the 0.3–10 keV unabsorbed flux measurements (or 3σ upper limits for nondetections).

We note that to derive M_{ej} and E_k as described above we assume the photospheric velocity evolution is negligible within 15 days relative to the peak epoch, and use the spectral velocities measured within this time frame to estimate $v_{\text{ph, max}}$ in Equation (1). However, there are four objects in our sample (SN 2018hom, SN 2018hxo, SN 2020tkx, and SN 2021hyz) for which the spectroscopic analysis constrained the photospheric velocity only after day 15 relative to the peak epoch. For these events, we only provide lower limits on the ejecta mass and kinetic energy (see Table 5).

Considering only the SNe in our sample for which we are able to measure the photospheric velocity within 15 days since the peak epoch, we derive median values for the ejecta masses and kinetic energies of $1.7 M_\odot$ and 2.2×10^{51} erg, respectively. These are both a factor of ≈ 2 smaller than the median values derived for the PTF/iPTF sample of SNe Ic-BL (Taddia et al. 2019). This could be due to either an intrinsic effect, or to uncertainties in the measured photospheric velocities. In fact, we note that the photospheric velocity is expected to decrease very quickly after maximum light (see, e.g., Figure 5). Since the photospheric velocity in Equation (1) of the Arnett formulation is the one at peak, our estimates of $v_{\text{ph, max}}$ could easily underestimate that velocity by a factor of ≈ 2 for many of the SNe in our sample. This would in turn yield an underestimate of M_{ej} by a factor of ≈ 2 (though the kinetic energy would be reduced by a larger factor). A more in-depth analysis of these trends and uncertainties will be presented in G. P. Srinivasaragavan et al. (2023, in preparation).

3.3. Search for Gamma-Rays

Based on the explosion dates derived for each object in Section 3.2 (Table 5), we searched for potential GRB coincidences in several online archives. No potential counterparts were identified in both spatial and temporal coincidence with either the Burst Alert Telescope (BAT; Barthelmy et al. 2005) on the Neil Gehrels Swift Observatory²⁷ or the Gamma-ray Burst Monitor (GBM; Meegan et al. 2009) on Fermi.²⁸

Several candidate counterparts were found with temporal coincidence in the online catalog from the KONUS instrument on the Wind satellite (SN 2018etk, SN 2018hom, SN 2019xcc, SN 2020jqm, SN 2020lao, SN 2020tkx, and SN 2021aug). However, given the relatively imprecise explosion date constraints for several of the events in our sample (see Table 5), and the coarse localization information from the KONUS instrument, we cannot firmly associate any of these GRBs with the SNe Ic-BL. In fact, given the rate of GRB detections by KONUS ($\sim 0.42 \text{ d}^{-1}$) and the time window over which we searched for counterparts (30 days in total; derived from the explosion date constraints), the observed number of coincidences (13) is consistent with random fluctuations. Finally, none of the possible coincidences were identified in events with the explosion date constraints more precise than 1 day.

3.4. X-Ray Constraints

Seven of the nine SNe Ic-BL observed with Swift-XRT did not result in a significant detection. In Table 4 we report the derived 90% confidence flux upper limits in the 0.3–10 keV band after correcting for Galactic absorption (Willingale et al. 2013).

While observations of SN 2021ywf resulted in a $\approx 3.2\sigma$ detection significance (Gaussian equivalent), the limited number of photons (eight) precluded a meaningful spectral fit. Thus, a $\Gamma = 2$ power-law spectrum was adopted for the flux conversion for this source as well. We note that because of the relatively poor spatial resolution of Swift-XRT (estimated positional uncertainty of $9''$ radius at 90% confidence), we cannot entirely rule out unrelated emission from the host galaxy of SN 2021ywf (e.g., active galactic nuclei, X-ray binaries, diffuse host emission, etc.; see Figure 6).

For SN 2019hsx we detected enough photons to perform a spectral fit for count rate to flux conversion. The spectrum is found to be relatively soft, with a best-fit power-law index of $\Gamma = 3.9^{+3.0}_{-2.1}$. Our Swift observations of SN 2019hsx do not show significant evidence for variability of the source X-ray

²⁷ See <https://swift.gsfc.nasa.gov/results/batgrbrcat>

²⁸ See <https://heasarc.gsfc.nasa.gov/W3Browse/fermi/fermigbrst.html>

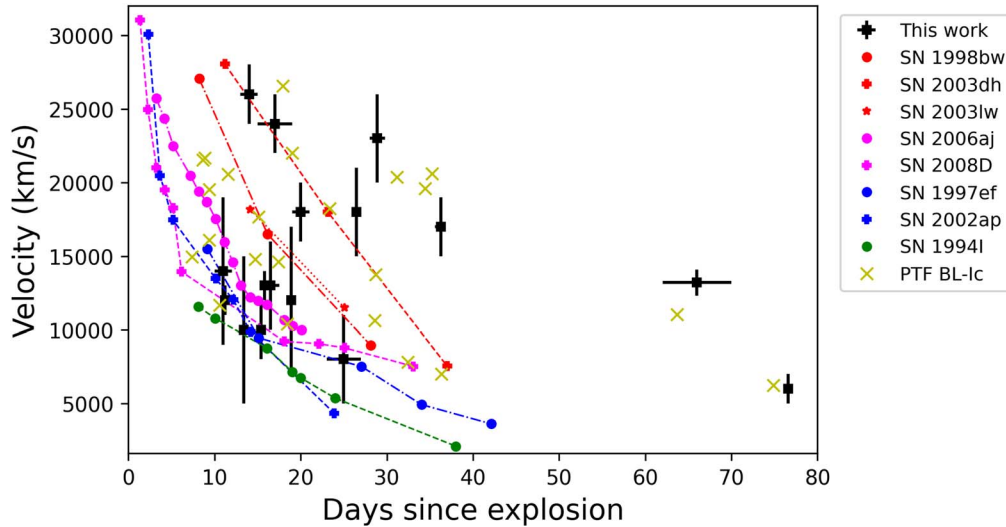


Figure 5. Photospheric velocities of the ZTF SNe in our sample (black) plotted as a function of (rest-frame) time since explosion (see Table 5). Velocities are measured using Fe II 5169 Å; velocities quoted refer to 84% confidence and are measured relative to the Ic template velocity using the open source software *SESNSpectralLib* (Liu et al. 2016; Modjaz et al. 2016). We compare our results with photospheric velocities derived from spectroscopic modeling for a number of SNe Ib/c. Red symbols represent GRB-SNe (Iwamoto et al. 1998; Mazzali et al. 2003, 2006a); magenta is used for XRF/X-ray transients SNe (Mazzali et al. 2006b; Pian et al. 2006; Modjaz et al. 2009); blue represents SNe Ic-BL (Mazzali et al. 2000, 2002); and green is used for the “normal” Type Ic SN 1994I (Sauer et al. 2006). Finally, for comparison we also plot the photospheric velocities for the SNe Ic-BL in the Corsi et al. (2016) sample as measured by Taddia et al. (2019; see their Tables 2 and A1; yellow crosses). Errors on the times since explosion account for the uncertainties on as reported in Table 5.

flux over the timescales of our follow up. While the lack of temporal variability is not particularly constraining given the low signal-to-noise ratios of individual epochs, we caution that also in this case the relatively poor spatial resolution of Swift-XRT (6.6 radius position uncertainty at 90% confidence) implies that unrelated emission from the host galaxy cannot be excluded (see Figure 6).

The constraints derived from the Swift-XRT observations can be compared with the X-ray light curves of low-luminosity GRBs, or models of GRB afterglows observed slightly off-axis. For the latter, we use the numerical model by van Eerten & MacFadyen (2011) and van Eerten et al. (2012). We assume equal energies in the electrons and magnetic fields ($\epsilon_B = \epsilon_e = 0.1$), and an interstellar medium (ISM) of density $n = 1\text{--}10\text{ cm}^{-3}$. We note that a constant-density ISM (rather than a wind profile) has been shown to fit the majority of GRB afterglow light curves, implying that most GRB progenitors might have relatively small wind termination-shock radii (Schulze et al. 2011). We generate the model light curves for a nominal redshift of $z = 0.05$ and then convert the predicted flux densities into X-ray luminosities by integrating over the 0.3–10 keV energy range and neglecting the small redshift corrections. We plot the model light curves in Figure 7, for various energies, different power-law indices p of the electron energy distribution, and various off-axis angles (relative to a jet opening angle, set to $\theta_j = 0.2$). In the same figure we also plot the X-ray light curves of low-luminosity GRBs for comparison (neglecting redshift corrections). As evident from this figure, our Swift/XRT upper limits (downward-pointing triangles) exclude X-ray afterglows associated with higher-energy GRBs observed slightly off-axis. However, X-ray emission as faint as the afterglow of the low-luminosity GRB 980425 cannot be excluded. As we discuss in the next section, radio data collected with the VLA enable us to exclude GRB 980425/SN 1998bw-like emission for most of the SNe in our sample.

3.5. Radio Constraints

As evident from Table 2, we have obtained at least one radio detection for 11 of the 16 SNe in our sample. None of these 11 radio sources were found to be coincident with known radio sources in the VLA FIRST (Becker et al. 1995) catalog (using a search radius of 30'' around the optical SN positions). This is not surprising since the FIRST survey had a typical rms sensitivity of $\approx 0.15\text{ mJy}$ at 1.4 GHz, much shallower than the deep VLA follow-up observations carried out within this follow-up program. We also checked the quick look images from the VLA Sky Survey (VLASS), which reach a typical rms sensitivity of $\approx 0.12\text{ mJy}$ at 3 GHz (Law et al. 2018; Villarreal Hernández & Andernach 2018). We could find images for all but one (SN 2021epp) of the fields containing the 16 SNe BL-Ic in our sample. The VLASS images did not provide any radio detection at the locations of the SNe in our sample.

Five of the 11 SNe Ic-BL with radio detections are associated with extended or marginally resolved radio emission. Two other radio-detected events (SN 2020rph and SN 2021hyz) appear point-like in our images, but show no evidence for significant variability of the detected radio flux densities over the timescales of our observations. Thus, for a total of seven out of 11 SNe Ic-BL with radio detections (see Figure 8), we consider the measured flux densities as upper limits corresponding to the brightnesses of their host galaxies, similarly to what was done in, e.g., Soderberg et al. (2006a) and Corsi et al. (2016). The remaining four SNe Ic-BL with radio detections (Figure 9) are compatible with point sources (SN 2018hom, SN 2020jqm, SN 2020tkx, and SN 2021ywf), and all but one (SN 2018hom) had more than one observation in the radio via which we were able to establish the presence of substantial variability of the radio flux density. Hereafter we consider these four detections as genuine radio SN counterparts, though we stress that with only one observation of SN 2018hom we cannot rule out a contribution from host-galaxy emission, especially given that the radio follow up of

Table 5
Optical Properties of the 16 SNe Ic-BL in Our Sample

SN	$T_{r,\max}$ (MJD)	M_r^{peak} (AB mag)	M_g^{peak} (AB mag)	$T_{\text{exp}} - T_{r,\max}$ (d)	M_{Ni} (M_{\odot})	τ_m (d)	$v_{\text{ph}}^{(a)}$ (10^4 km s^{-1})	M_{ej} (M_{\odot})	E_k (10^{51} erg)
2018etk	58337.40	-18.31 ± 0.03	-18.30 ± 0.02	-9 ± 1	$0.13^{+0.01}_{-0.02}$	5.0^{+2}_{-2}	2.6 ± 0.2 (5)	0.7 ± 0.5	3 ± 2
2018hom	58426.31	-19.30 ± 0.11	-18.91 ± 0.01	$-9.3^{+0.7}_{-0.4}$	0.4 ± 0.1	6.9 ± 0.2	1.7 ± 0.2 (27)	>0.7	>1
2018hxo	58403.76	-18.68 ± 0.06	-18.4 ± 0.1	$-28.6^{+0.2}_{-0.3}$	0.4 ± 0.2	6 ± 2	0.6 ± 0.1 (48)	>0.1	>0.02
2018jex	58457.01	-19.06 ± 0.02	-18.61 ± 0.04	-18.49 ± 0.04	$0.53^{+0.07}_{-0.06}$	13^{+2}_{-3}	1.8 ± 0.3 (8)	3 ± 1	7 ± 3
2019hsx	58647.07	-17.08 ± 0.02	-16.14 ± 0.04	$-15.6^{+0.4}_{-0.5}$	$0.07^{+0.01}_{-0.01}$	12 ± 1	1.0 ± 0.2 (-0.2)	1.6 ± 0.4	1.0 ± 0.5
2019xcc	58844.59	-16.58 ± 0.06	-15.6 ± 0.2	-11 ± 2	0.04 ± 0.01	$5.0^{+1.4}_{-0.9}$	2.4 ± 0.2 (6)	0.7 ± 0.3	2 ± 1
2020jqm	58996.21	-18.26 ± 0.02	-17.39 ± 0.04	-17 ± 1	$0.29^{+0.05}_{-0.04}$	18 ± 2	1.3 ± 0.3 (-0.5)	5 ± 1	5 ± 3
2020lao	59003.92	-18.66 ± 0.02	-18.55 ± 0.02	-11 ± 1	0.23 ± 0.01	7.7 ± 0.2	1.8 ± 0.2 (9)	1.2 ± 0.2	2.5 ± 0.7
2020rph	59092.34	-17.48 ± 0.02	-16.94 ± 0.03	-19.88 ± 0.02	0.07 ± 0.01	$17.23^{+1.2}_{-0.9}$	1.2 ± 0.5 (-1)	4 ± 2	3 ± 3
2020tkx	59116.50	-18.49 ± 0.05	-18.19 ± 0.03	-13 ± 4	0.22 ± 0.01	$10.9^{+0.7}_{-0.8}$	1.32 ± 0.09 (53)	>1.5	>1.5
2021xv	59235.56	-18.92 ± 0.07	-18.99 ± 0.05	$-12.8^{+0.2}_{-0.3}$	$0.30^{+0.01}_{-0.02}$	$7.7^{+0.7}_{-0.5}$	1.3 ± 0.1 (3)	0.9 ± 0.1	1.0 ± 0.2
2021aug	59251.98	-19.42 ± 0.01	-19.32 ± 0.06	-24 ± 2	0.7 ± 0.1	17 ± 7	0.8 ± 0.3 (1)	3 ± 2	1 ± 1
2021epp	59291.83	-17.49 ± 0.03	-17.12 ± 0.09	-15 ± 1	0.12 ± 0.02	17^{+4}_{-3}	1.4 ± 0.5 (-4)	5 ± 2	6 ± 5
2021htb	59321.56	-16.55 ± 0.03	-15.66 ± 0.07	-19.38 ± 0.02	0.04 ± 0.01	13 ± 2	1.0 ± 0.5 (-6)	1.8 ± 0.9	1 ± 1
2021hyz	59319.10	-18.83 ± 0.05	-18.81 ± 0.01	-12.9 ± 0.9	$0.29^{+0.01}_{-0.02}$	$7.7^{+0.5}_{-0.4}$	2.3 ± 0.3 (16)	>1.3	>4
2021ywf	59478.64	-17.10 ± 0.05	-16.5 ± 0.1	-10.7 ± 0.5	0.06 ± 0.01	8.9 ± 0.8	1.2 ± 0.1 (0.5)	1.1 ± 0.2	0.9 ± 0.3

Note. We list the SN name; the MJD of maximum light in r band; the absolute magnitude at r -band peak; the absolute magnitude at g -band peak; the explosion time estimated as days since r -band maximum (in the source's rest frame); the estimated nickel mass; the characteristic timescale of the bolometric light curve; the photospheric velocity; the ejecta mass; and the kinetic energy of the explosion. See Sections 3.1 and 3.2 for discussion.

^a Rest-frame phase days of the spectrum that was used to measure the velocity.

this event was carried out with the VLA in its most compact (D) configuration with poorer angular resolution.

In summary, our radio follow-up campaign of 16 SNe Ic-BL resulted in four radio counterpart detections, and 12 deep upper limits on associated radio counterparts.

3.5.1. Fraction of SN 1998bw-like SNe Ic-BL

The local rate of SNe Ic-BL is estimated to be $\approx 5\%$ of the core-collapse SN rate (Li et al. 2011; Shivvers et al. 2017) or $\approx 5 \times 10^3 \text{ Gpc}^{-3} \text{ yr}^{-1}$ assuming a core-collapse SN rate of $\approx 10^5 \text{ Gpc}^{-3} \text{ yr}^{-1}$ (Perley et al. 2020). Observationally, we know that cosmological long GRBs are characterized by ultrarelativistic jets observed on-axis, and have an intrinsic (corrected for beaming angle) local volumetric rate of $79^{+57}_{-33} \text{ Gpc}^{-3} \text{ yr}^{-1}$ (e.g., Ghirlanda & Salvaterra 2022, and references therein). Hence, only $\mathcal{O}(1)\%$ of SNe Ic-BL can make long GRBs. For low-luminosity GRBs, the observed local rate is affected by large errors, $230^{+490}_{-190} \text{ Gpc}^{-3} \text{ yr}^{-1}$ (see Bromberg et al. 2011, and references therein), and their typical beaming angles are largely unconstrained. Hence, the question of what fraction of SNe Ic-BL can make low-luminosity GRBs remains to be answered.

Radio observations of SNe Ic-BL are a powerful way to constrain this fraction independently of relativistic beaming effects that preclude observations of jets in X-rays and γ -rays for off-axis observers. However, observational efforts aimed at constraining the fraction of SNe Ic-BL harboring low-luminosity GRBs independently of γ -ray observations have long been challenged by the rarity of the SN Ic-BL optical detections (compared to other core-collapse events), coupled with the small number of these rare SNe for which the community has been able to collect deep radio follow-up observations within 1 yr since explosion (see, e.g., Soderberg et al. 2006b). Progress in this respect has been made since the advent of the PTF, and more generally with synoptic optical

surveys that have greatly boosted the rate of stripped-envelope core-collapse SN discoveries (e.g., Shappee et al. 2014; Tonry et al. 2018d; Sand et al. 2018).

In our previous work (Corsi et al. 2016), we presented one of the most extensive samples of SNe Ic-BL with deep VLA observations, largely composed of events detected by PTF/iPTF. Combining our sample with the SN Ic-BL 2002ap (Gal-Yam et al. 2002; Mazzali et al. 2002) and SN 2002bl (Armstrong 2002; Berger et al. 2003), and the circumstellar medium (CSM)-interacting SN Ic-BL 2007bg (Salas et al. 2013), we had overall 16 SNe Ic-BL for which radio emission observationally similar to SN 1998bw was excluded, constraining the rate of SNe Ic-BL observationally similar to SN 1998bw to $<6.61/16 \approx 41\%$, where we have used the fact that the Poisson 99.865% confidence (or 3σ Gaussian equivalent for a single-sided distribution) upper limit on zero SNe compatible with SN 1998bw is ≈ 6.61 .

With the addition of the 16 ZTF SNe Ic-BL presented in this work, we now have doubled the sample of SNe Ic-BL with deep VLA observations presented in Corsi et al. (2016), providing evidence for additional 15 SNe Ic-BL (all but SN 2021epp; see Figure 10) that are observationally different from SN 1998bw in the radio. Adding to our sample also SN 2018bvw (Ho et al. 2020a), AT 2018gep (Ho et al. 2019), and SN 2020bvc (Ho et al. 2020b), whose radio observations exclude SN 1998bw-like emission, we are now at 34 SNe Ic-BL that are observationally different from SN 1998bw. Hence, we can tighten our constraint on the fraction of 1998bw-like SNe Ic-BL to $<6.61/34 \approx 19\%$ (99.865% confidence). This upper limit implies that the intrinsic rate of 1998bw-like GRBs is $\lesssim 950 \text{ Gpc}^{-3} \text{ yr}^{-1}$. Combining this constraint with the rate of low-luminosity GRBs derived from their high-energy emission, we conclude that low-luminosity GRBs have inverse beaming factors $2/\theta^2 \lesssim 4^{+20}_{-3}$, corresponding to jet half-opening angles $\theta \gtrsim 40^{+40}_{-24} \text{ deg}$.

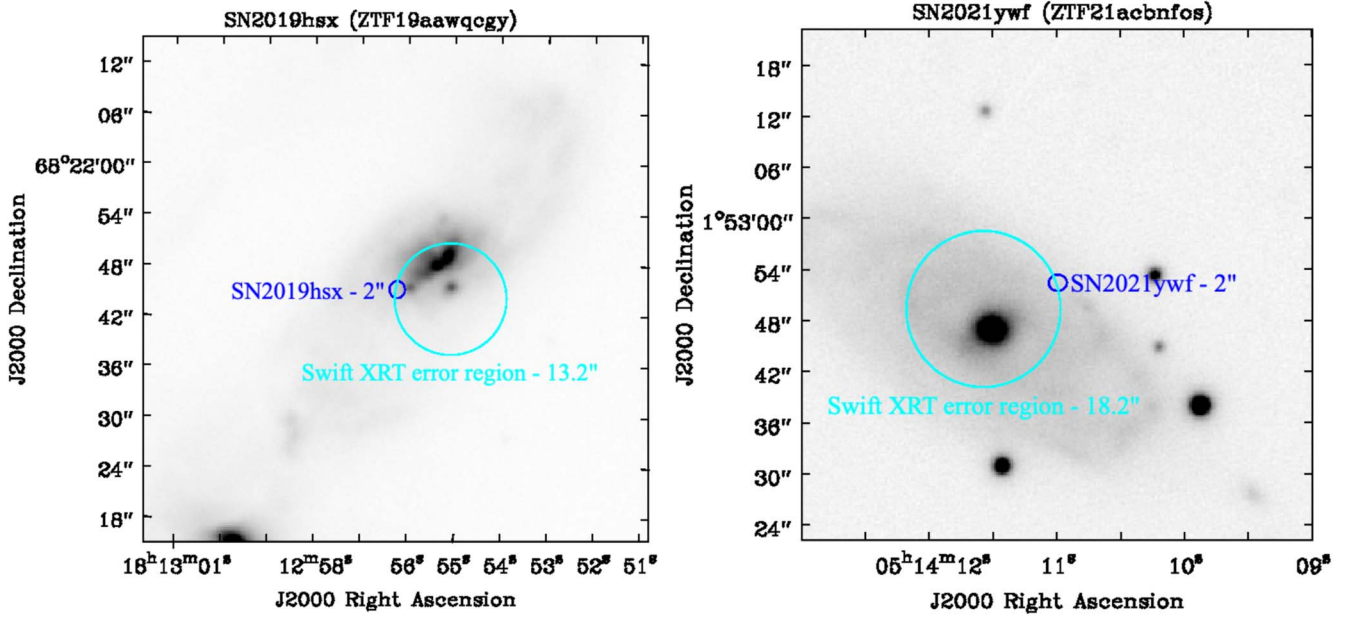


Figure 6. Pan-STARRS-1 (Flewelling et al. 2020) reference r -band images of the fields of the SNe in our sample for which we have a detection with Swift/XRT (see Table 4). The blue circles centered on the optical SN positions (not shown in the images) have sizes of $2''$ (comparable to the ZTF point-spread function (PSF) at average seeing; Bellm et al. 2019). The cyan circles are centered on the XRT position and enclose the 90% XRT error region.

For 10 of the SNe in the sample presented here we also exclude relativistic ejecta with radio luminosity densities in between $\approx 5 \times 10^{27} \text{ erg s}^{-1} \text{ Hz}^{-1}$ and $\approx 10^{29} \text{ erg s}^{-1} \text{ Hz}^{-1}$ at $t \gtrsim 20$ days, pointing to the fact that SNe Ic-BL similar to those associated with low-luminosity GRBs, such as SN 1998bw (Kulkarni et al. 1998), SN 2003lw (Soderberg et al. 2004), SN 2010bh (Margutti et al. 2013), or to the relativistic SN 2009bb (Soderberg et al. 2010) and iPTF17cw (Corsi et al. 2017), are intrinsically rare. We note that these constraints could be greatly improved in the future with more systematic VLA follow-up campaigns (e.g., via large VLA programs). Indeed, the sample of SNe Ic-BL discussed here is only about $\approx 39\%$ of the total sample of ZTF Ic-BL events presented in G. P. Srinivasaragavan et al. (2023, in preparation). Moreover, we note that none of our observations exclude radio emission similar to that of SN 2006aj. This is not surprising since the afterglow of this low-luminosity GRB faded on timescales much faster than the 20–30 days since explosion that our VLA monitoring campaign allowed us to target. To enable progress, obtaining prompt ($\lesssim 5$ days since explosion) and accurate spectral classification paired with deep radio follow-up observations of SNe Ic-BL should be a major focus of future studies. At the same time, as discussed in Ho et al. (2020b), high-cadence optical surveys can provide an alternative way to measure the rate of SNe Ic-BL that are similar to SN 2006aj independently of γ -ray and radio observations, by catching potential optical signatures of shock-cooling emission at early times. Based on an analysis of ZTF SNe with early high-cadence light curves, Ho et al. (2020b) concluded that it appears that SN 2006aj-like events are uncommon, but more events will be needed to measure a robust rate.

3.5.2. Properties of the Radio-emitting Ejecta

While none of the SNe in our sample for which we obtained a radio detection shows evidence for ejecta as relativistic as that of SN 1998bw, hereafter we aim to better constrain their radio properties within the synchrotron self-absorption (SSA) model

for radio SNe (Chevalier 1998). Within this model, the measured radio peak frequency and peak flux can provide information on the size of the radio-emitting material (and hence its speed), as well as on the mass-loss rate of the SN progenitor. We start from Equations (11) and (13) of Chevalier (1998):

$$R_p \approx 8.8 \times 10^{15} \text{ cm} \left(\frac{\eta}{2\alpha} \right)^{1/(2p+13)} \left(\frac{F_p}{\text{Jy}} \right)^{(p+6)/(2p+13)} \times \left(\frac{d_L}{\text{Mpc}} \right)^{(2p+12)/(2p+13)} \left(\frac{\nu_p}{5 \text{ GHz}} \right)^{-1}, \quad (2)$$

where $\alpha \approx 1$ is the ratio of relativistic electron energy density to magnetic energy density, F_p is the flux density at the time of SSA peak, ν_p is the SSA frequency, and where R/η is the thickness of the radiating electron shell. The normalization of the above Equation has a small dependence on p and in the above we assume $p \approx 3$ for the power-law index of the electron energy distribution. Setting $R_p \approx v_s t_p$ in Equation (2), and considering that $L_p \approx 4\pi d_L^2 F_p$ (neglecting redshift effects), we get:

$$\left(\frac{L_p}{\text{erg s}^{-1} \text{ Hz}^{-1}} \right) \approx 1.2 \times 10^{27} \left(\frac{\beta_s}{3.4} \right)^{(2p+13)/(p+6)} \times \left(\frac{\eta}{2\alpha} \right)^{-1/(p+6)} \left(\frac{\nu_p}{5 \text{ GHz}} \frac{t_p}{1 \text{ day}} \right)^{(2p+13)/(p+6)}, \quad (3)$$

where we have set $\beta_s = v_s/c$. We plot in Figure 11 with blue dotted lines the relationship above for various values of β_s (and for $p = 3$, $\eta = 2$, and $\alpha = 1$). As evident from this figure, relativistic events such as SN 1998bw (for which the

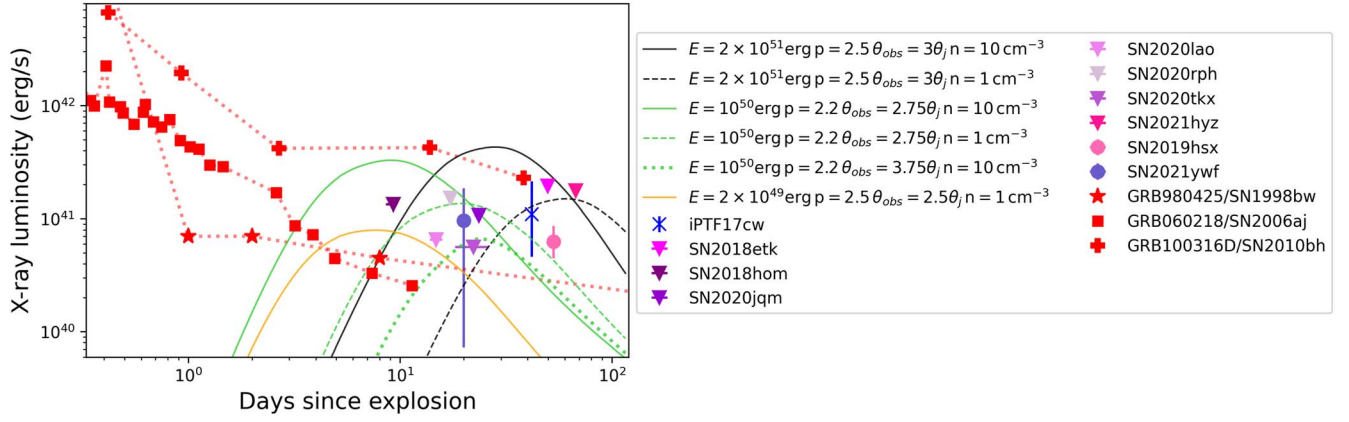


Figure 7. Swift/XRT upper limits and detections (downward-pointing triangles and filled circles with error bars, respectively) obtained for nine of the 16 SNe Ic-BL in our sample. We plot the observed X-ray luminosity as a function of time since explosion. We compare these observations with the X-ray light curves of the low-luminosity GRBs 980425 (red stars; Kouveliotou et al. 2004), 060218 (red squares; Campana et al. 2006), and 100316D (red crosses; Margutti et al. 2013), and with the relativistic iPTF17cw (blue cross; Corsi et al. 2017). Dotted red lines connect the observed data points (some of which at early and late times are not shown in the plot) for these three low-luminosity GRBs. We also plot the observed X-ray luminosity predicted by off-axis GRB models (black, green, and orange lines; van Eerten & MacFadyen 2011; van Eerten et al. 2012). We assume $\epsilon_B = \epsilon_e = 0.1$, a constant-density ISM in the range $n = 1\text{--}10\text{ cm}^{-3}$, a top-hat jet of opening angle $\theta_j = 0.2$, and various observer angles $\theta_{\text{obs}} = (2.5\text{--}3)\theta_j$.

nonrelativistic approximation used in the above equations breaks down) are located at $\beta_s \gtrsim 1$.

To estimate the speed of the radio-emitting ejecta of the four SNe for which we have a radio detection, we use Equation (3) above and our radio measurements to place each of these four SNe in Figure 11. In doing so, the following considerations are relevant. For SN 2018hom, we only have one radio observation. Hence, contamination from the host galaxy cannot be excluded, and we cannot really constrain the time of the peak and peak luminosity at the observed frequency. However, if the luminosity we measure at the time of our observation is close to the peak and dominated by SN emission, then the implied ejecta speed is $\approx 0.3c$ (Figure 11). For SN 2020tkx, we have three observations that indicate a rise followed by a decay in the observed flux at 10 GHz over the corresponding epochs (the third observation is at 5 GHz, but for optically thin emission we expect the flux at 10 GHz to be less than that measured at 5 GHz at the same epoch; see Table 3). Hence, we constrain the emission peak to be at 10 GHz at $\approx 33\text{--}71$ days after explosion (see Tables 5 and 3). Moreover, our two 10 GHz observations indicate a relatively flat rise of the luminosity density ($L \propto t^a$ with $a \approx 0.85$) when compared with the theoretical expectations for the optically thick prepeak evolution of $L \propto t^a$ with $a \approx 1.7\text{--}2.5$ (see the discussion for model 1 and model 4 in Section 2 of Chevalier 1998). Hence, it is reasonable to assume that the light curve at 10 GHz is already flattening at ≈ 33 days since explosion, indicating that ν_p is likely passing in band around that epoch. In Figure 11, we show the constraint derived assuming a peak epoch of ≈ 33 days. In the case of SN 2020jqm, its double-peaked radio light curve yields two possible estimates of the ejecta speed, potentially associated with two different ejecta shells interacting with the CSM (similarly to the case of PTF11qej; see e.g., Corsi et al. 2014; Palliyaguru et al. 2019). We report in Figure 11 both these estimates. We note that the second radio peak is assumed to occur at the time of our last observation of SN 2020jqm, and yields an ejecta speed that suggests radio-loud CSM interaction similar to PTF11qej. Finally, in the case of SN 2021ywf, our observations show a decreasing radio light curve, $L \propto t^{-b}$ with $b \approx 0.65$, indicating that the peak occurred at $\lesssim 19$ days since explosion. Considering

the fastest-evolving radio-emitting Ic-BL SN we know of (SN 2006aj), it is reasonable to assume 5 days $\lesssim t_p \lesssim 19$ days at 5 GHz. In Figure 11, we show the constraint derived on the ejecta speed of SN 2021ywf setting $t_p \approx 19$ d. For $p = 3$, an earlier peak time of 5 days would imply a radio ejecta speed $\approx (5/19)^{-1.3} \times$ higher than the value of $\approx 0.19c$ shown in Figure 11. Hence, for this event we cannot exclude relativistic radio ejecta with speed comparable to that of iPTF17cw.

Our radio measurements can also be used to get an estimate of the SN progenitor mass-loss rate. To this end, we note that in the SSA model the magnetic field can be expressed as (see Equations (12) and (14) in Chevalier 1998):

$$B_p \approx 0.58 \text{ G} \left(\frac{\eta}{2\alpha} \right)^{4/(2p+13)} \left(\frac{F_p}{\text{Jy}} \right)^{-2/(2p+13)} \times \left(\frac{d_L}{\text{Mpc}} \right)^{-4/(2p+13)} \left(\frac{\nu_p}{5 \text{ GHz}} \right). \quad (4)$$

Now consider an SN shock expanding in a CSM of density:

$$\rho \approx 5 \times 10^{11} \text{ g cm}^{-3} A_* R^{-2}, \quad (5)$$

where:

$$A_* = \frac{\dot{M}/(10^{-5} M_\odot \text{ yr}^{-1})}{4\pi v_w/(10^3 \text{ km s}^{-1})}. \quad (6)$$

Assuming that a fraction ϵ_B of the energy density ρv_s^2 goes into magnetic fields:

$$\frac{B_p^2}{8\pi} = \epsilon_B \rho v_s^2 = \epsilon_B \rho R_p^2 t_p^{-2}, \quad (7)$$

one can write:

$$\left(\frac{L_p}{\text{erg s}^{-1} \text{ Hz}^{-1}} \right) \approx 1.2 \times 10^{27} \left(\frac{\eta}{2\alpha} \right)^2 \left(\frac{\nu_p}{5 \text{ GHz}} \frac{t_p}{1 \text{ day}} \right)^{(2p+13)/4} \times (5 \times 10^3 \epsilon_B A_*)^{-(2p+13)/4}, \quad (8)$$

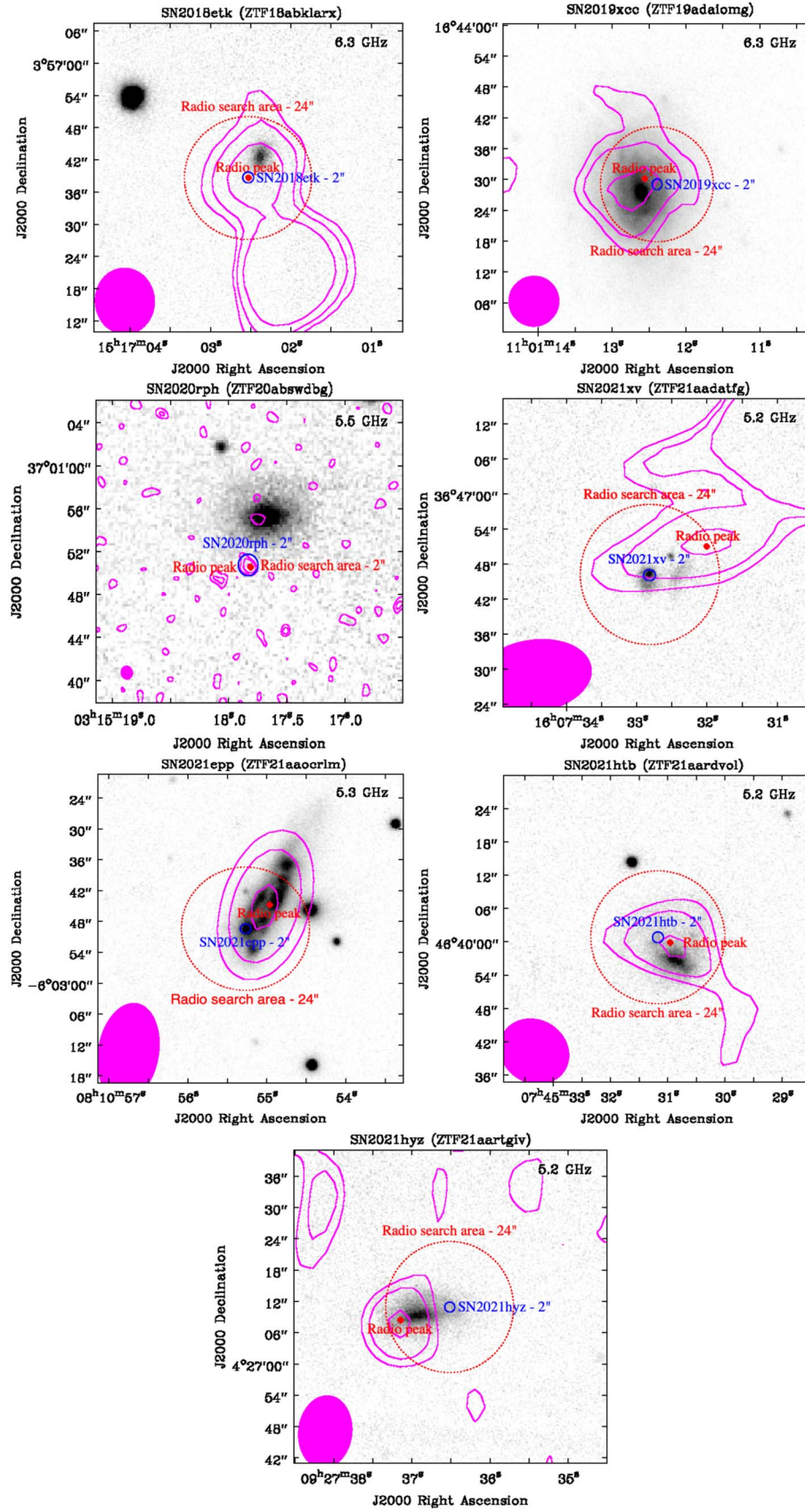


Figure 8. Pan-STARRS-1 (Flewelling et al. 2020) reference *r*-band images of the fields of the SNe in our sample for which host-galaxy light dominates the radio emission. Contours in magenta are 30%, 50%, and 90% of the radio peak flux reported in Table 2 for the first radio detection of each field. The blue circles centered on the optical SN positions (not shown in the images) have sizes of 2" (comparable to the ZTF PSF at average seeing; Bellm et al. 2019). The red dotted circles enclose the region in which we search for radio counterparts (radii equal to the nominal FWHM of the VLA synthesized beams; Table 2). The sizes of the actual VLA synthesized beams are shown as filled magenta ellipses. The red dots mark the locations of the radio peak fluxes measured in the radio search areas.

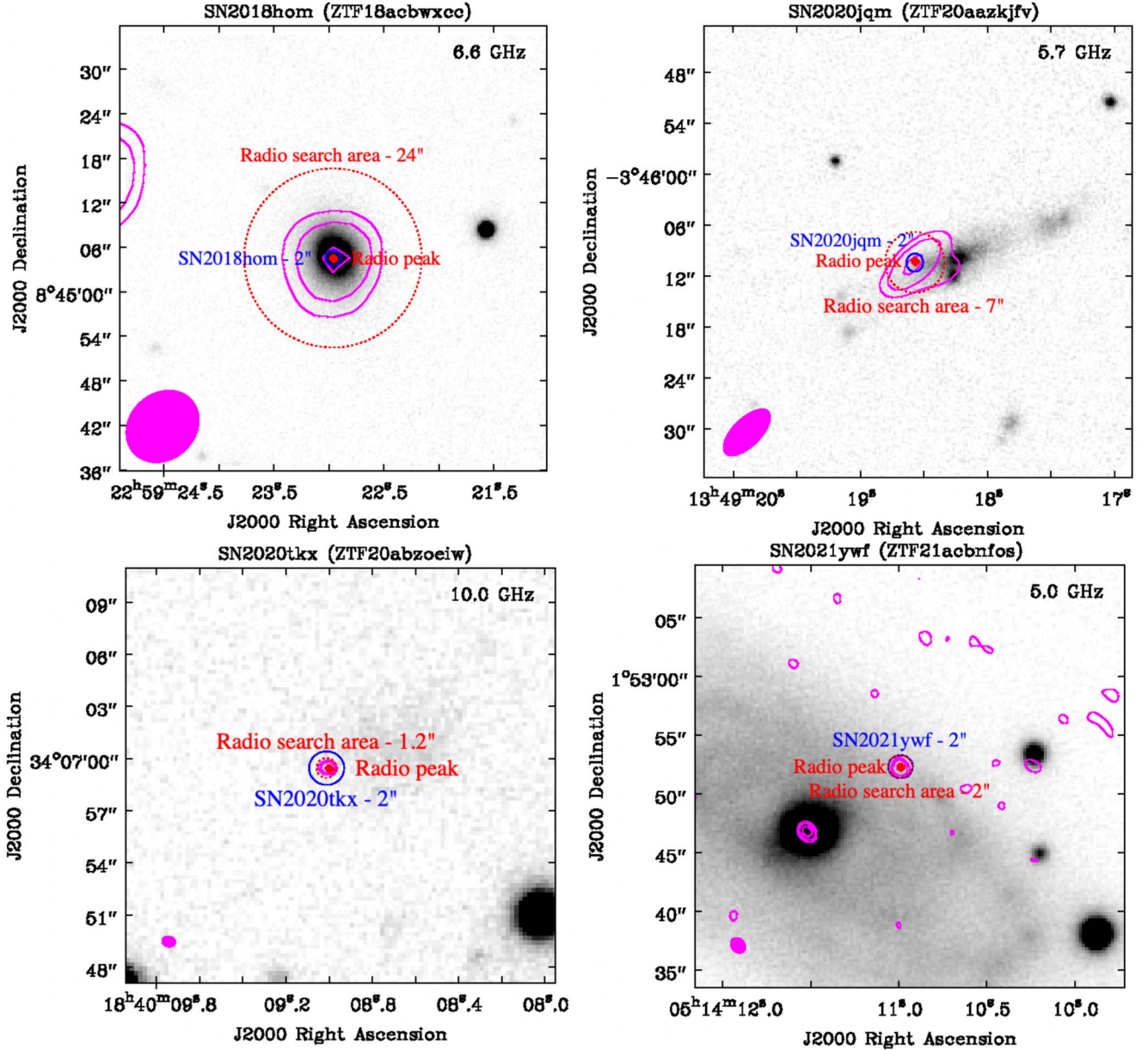


Figure 9. Same as Figure 8 but for the fields containing the SNe in our sample for which we detected an SN radio counterpart. We stress that with only one observation of SN 2018hom we cannot rule out a contribution from host-galaxy emission, especially given that the radio follow up of this event was carried out with the VLA in its D configuration.

where we have used Equations (4), (6), and (7). We plot in Figure 11 with yellow dashed lines the relationship above for various values of \dot{M} (and for $p = 3$, $\eta = 2$, $\alpha = 1$, $\epsilon_B = 0.33$, and $v_w = 1000 \text{ km s}^{-1}$). As evident from this figure, relativistic events such as SN 1998bw show a preference for smaller mass-loss rates. We note that while the above relationship depends strongly on the assumed values of η , ϵ_B , and v_w , this trend for \dot{M} remains true regardless of the specific values of these (uncertain) parameters. We also note that the above analysis assumes mass loss in the form of a steady wind. While this is generally considered to be the case for relativistic SNe Ic-BL, binary interaction or eruptive mass loss in core-collapse SNe can produce denser CSMs with more complex profiles (e.g., Montes et al. 1998; Soderberg et al. 2006a; Salas et al. 2013; Corsi et al. 2014;

Margutti et al. 2017; Balasubramanian et al. 2021; Maeda et al. 2021; Strohm et al. 2021).

Finally, the total energy coupled to the fastest (radio-emitting) ejecta can be expressed as (e.g., Soderberg et al. 2006a):

$$E_r \approx \frac{4\pi R_p^3}{\eta} \frac{B_p^2}{8\pi\epsilon_B} = \frac{R_p^3}{\eta} \frac{B_p^2}{2\epsilon_B}. \quad (9)$$

In Table 3 we summarize the properties of the radio ejecta derived for the four SNe for which we detect a radio counterpart. These values can be compared with $\dot{M} \approx 2.5 \times 10^{-7} M_\odot \text{ yr}^{-1}$ and $E_r \approx (1-10) \times 10^{49} \text{ erg}$ estimated for SN 1998bw by Li & Chevalier (1999), with $\dot{M} \approx 2 \times 10^{-6} M_\odot \text{ yr}^{-1}$ and $E_r \approx 1.3 \times 10^{49} \text{ erg}$ estimated for SN 2009bb by Soderberg et al. (2010), and with with

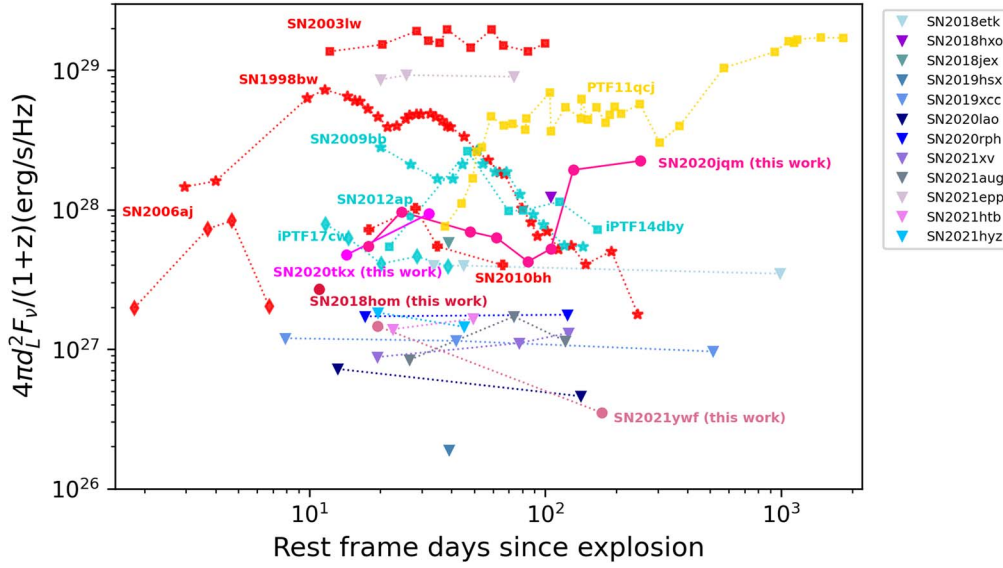


Figure 10. Radio (≈ 6 GHz) observations of the 16 SNe Ic-BL in our sample (filled circles and downward-pointing triangles in shades of pink, purple, and blue). Upper limits associated with nondetections (3σ or brightness of the host galaxy at the optical location of the SN) are plotted with downward-pointing triangles; detections are plotted with filled circles. We compare these observations with the radio light curves of GRB-SNe (red), of relativistic-to-mildly relativistic SNe Ic-BL discovered independently of a γ -ray trigger (cyan), and with PTF11qej (Corsi et al. 2014), an example of a radio-loud nonrelativistic and CSM-interacting SN Ic-BL (yellow). As evident from this figure, our observations exclude SN 1998bw-like radio emission for all but one (SN 2021epp) of the events in our sample. This doubles the sample of SNe Ic-BL for which radio emission observationally similar to SN 1998bw was previously excluded (Corsi et al. 2016), bringing the upper limit on the fraction of SNe compatible with SN 1998bw down to $<19\%$ (compared to $<41\%$ previously reported in Corsi et al. 2016). For 10 of the 16 SNe presented here we also exclude relativistic ejecta with radio luminosity densities in between $\approx 5 \times 10^{27} \text{ erg s}^{-1} \text{ Hz}^{-1}$ and $\approx 10^{29} \text{ erg s}^{-1} \text{ Hz}^{-1}$ at $t \gtrsim 20$ days, similar to SNe associated with low-luminosity GRBs such as SN 1998bw (Kulkarni et al. 1998), SN 2003lw (Soderberg et al. 2004), SN 2010bh (Margutti et al. 2013), or to the relativistic SN 2009bb (Soderberg et al. 2010) and iPTF17cw (Corsi et al. 2017). None of our observations exclude radio emission similar to that of SN 2006aj.

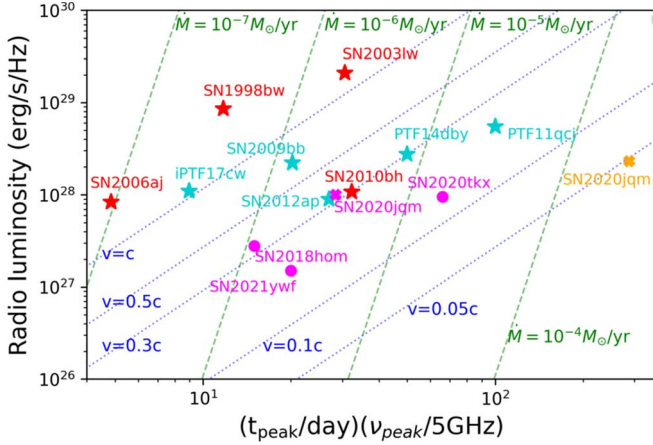


Figure 11. Properties of the radio-emitting ejecta of the SNe in our sample for which we detect a radio counterpart (magenta dots, magenta cross, and orange cross), compared with those of GRB-SNe (red stars) and of relativistic-to-mildly relativistic SNe Ic-BL discovered independently of a γ -ray trigger (cyan stars). SN 2018hom is compatible with an ejecta speed $\gtrsim 0.3c$, though with the caveat that we only have one radio observation for this SN. SN 2020jmq has a double-peaked radio light curve and we estimate the radio ejecta speed associated with each of these two peaks. We note that the second radio peak places SN 2020jmq in the region of the parameter space occupied by radio-loud CSM-interacting SNe similar to PTF11qej (orange cross). Finally, for SN 2021ywf we can only set a lower limit on the ejecta speed ($\gtrsim 0.19c$) and we cannot exclude a faster ejecta similar to that of iPTF17cw. See Section 3.5.2 for discussion.

$\dot{M} \approx (0.4 - 1) \times 10^{-5} M_{\odot} \text{ yr}^{-1}$ and $E_r \approx (0.3 - 4) \times 10^{49} \text{ erg}$ estimated for GRB 100316D by Margutti et al. (2013).

3.5.3. Off-axis GRB Afterglow Constraints

The two X-ray detections of SN 2019hsx and SN 2021ywf shown in Figure 7 are consistent with several GRB off-axis

light curve models and, in the case of SN 2021ywf, also with GRB 980425-like emission within the large errors. However, for this interpretation of their X-ray emission to be compatible with our radio observations (see Table 2), one needs to invoke a flattening of the radio-to-X-ray spectrum, similar to what has been invoked for other stripped-envelope SNe in the context of cosmic-ray-dominated shocks (Ellison et al. 2000; Chevalier & Fransson 2006).

Hereafter, we finally consider what type of constraints our radio observations put on a scenario where the SNe Ic-BL in our sample could be accompanied by relativistic ejecta from a largely (close to 90°) off-axis GRB afterglow that would become visible in the radio band when the relativistic fireball enters the subrelativistic phase and approaches spherical symmetry. Because our radio observations do not extend past 100–200 days since explosion, we can put only limited constraints on this scenario. Hence, hereafter we present some general order-of-magnitude considerations rather than a detailed event-by-event modeling.

Following Corsi et al. (2016), we can model approximately the late-time radio emission from an off-axis GRB based on the results by Livio & Waxman (2000), Waxman (2004), Zhang & MacFadyen (2009), and van Eerten et al. (2012). For fireballs expanding in an ISM of constant density n (in units of cm^{-3}), at timescales t such that:

$$t \gtrsim (1+z) \times t_{\text{SNT}}/2, \quad (10)$$

where the transition time to the spherical Sedov–Neumann–Taylor (SNT) blast wave, t_{SNT} , reads:

$$t_{\text{SNT}} \approx 92 \text{ d} (E_{51}/n)^{1/3}, \quad (11)$$

the luminosity density can be approximated analytically via the following formula (see Equation (23) in Zhang &

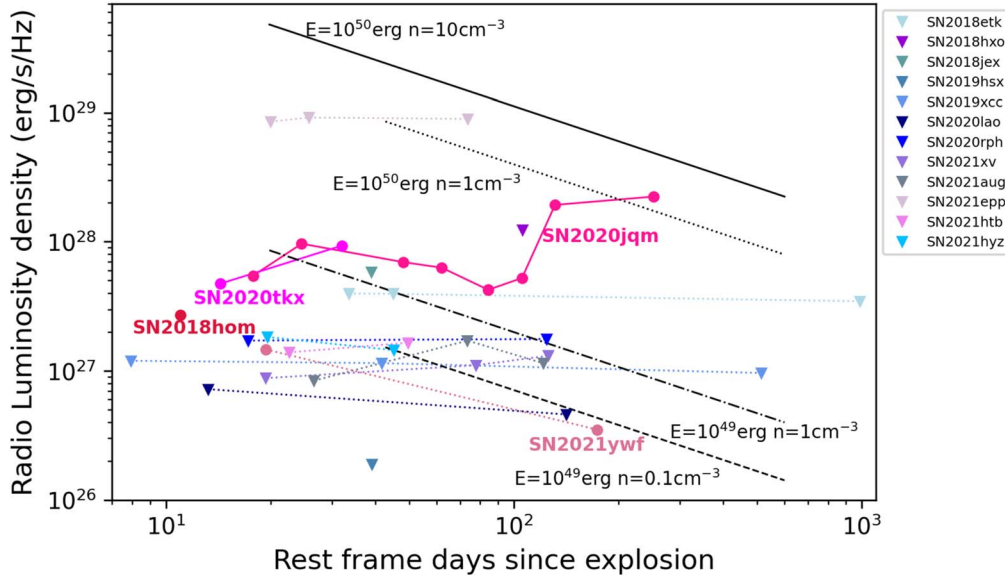


Figure 12. Approximate radio luminosity density for GRBs observed largely off-axis during the subrelativistic phase (black solid, dotted, dashed, and dashed-dotted lines) compared with the radio detections and upper limits of the SNe Ic-BL in our sample. Most of our observations exclude fireballs with energies $E \gtrsim 10^{50}$ erg expanding in ISMs with densities $\gtrsim 1 \text{ cm}^{-3}$. However, our observations become less constraining for smaller energies and ISM density values. For example, most of our radio data cannot exclude off-axis jets with energies $E \sim 10^{49}$ erg and $n \sim 0.1 \text{ cm}^{-3}$. See Section 3.5.3 for discussion.

MacFadyen 2009, where we neglect redshift corrections and assume $p = 2$):

$$L_\nu(t) \approx 4\pi d_L^2 F_\nu(t) \approx 2 \times 10^{30} \left(\frac{\epsilon_e}{0.1} \right) \left(\frac{\epsilon_B}{0.1} \right)^{3/4} n^{9/20} \times E_{51}^{13/10} \left(\frac{\nu}{1 \text{ GHz}} \right)^{-1/2} \left(\frac{t}{92 \text{ d}} \right)^{-9/10} \text{ erg s}^{-1} \text{ Hz}^{-1}. \quad (12)$$

In the above equations, E_{51} is the beaming-corrected ejecta energy in units of 10^{51} erg. We note that here we assume again a constant-density ISM in agreement with the majority of GRB afterglow observations (e.g., Schulze et al. 2011).

We plot the above luminosity in Figure 12 together with our radio observations and upper limits, assuming $\epsilon_e = 0.1$, $\epsilon_B = 0.1$, and for representative values of low-luminosity GRB energies and typical values of long GRB ISM densities n . As evident from this figure, our observations exclude fireballs with energies $E \gtrsim 10^{50}$ erg expanding in ISMs with densities $\gtrsim 1 \text{ cm}^{-3}$. However, our observations become less constraining for smaller energies and ISM density values.

4. Summary and Conclusion

We have presented deep radio follow-up observations of 16 SNe Ic-BL that are part of the ZTF sample. Our campaign resulted in four radio counterpart detections and 12 deep radio upper limits. For nine of these 16 events we have also carried out X-ray observations with Swift/XRT. All together, these results constrain the fraction of SN 1998bw-like explosions in the sample we have analyzed to $< 19\%$ (3σ Gaussian equivalent), tightening previous constraints by a factor of ≈ 2 . Moreover, our results exclude relativistic ejecta with radio luminosities densities in between $\approx 5 \times 10^{27} \text{ erg s}^{-1} \text{ Hz}^{-1}$ and $\approx 10^{29} \text{ erg s}^{-1} \text{ Hz}^{-1}$ at $t \gtrsim 20$ days since explosion for $\approx 60\%$ of the events in our sample, pointing to the fact that SNe Ic-BL similar to low-luminosity-GRB-SNe such as SN 1998bw, SN 2003lw, and SN 2010dh, or to the relativistic SNe 2009bb

and iPTF17cw, are intrinsically rare. This result is in line with numerical simulations that suggest that an SN Ic-BL can be triggered even if a jet engine fails to produce a successful GRB jet.

We showed that our radio observations exclude an association of the SNe Ic-BL in our sample with largely off-axis GRB afterglows with energies $E \gtrsim 10^{50}$ erg expanding in ISMs with densities $\gtrsim 1 \text{ cm}^{-3}$. On the other hand, our radio observations are less constraining for smaller energies and ISM density values, and cannot exclude off-axis jets with energies $E \sim 10^{49}$ erg.

We noted that the main conclusion of our work is subject to the caveat that the parameter space of SN 2006aj-like explosions (with faint radio emission peaking only a few days after explosion) is left largely unconstrained by current systematic radio follow-up efforts like the one presented here. In other words, we cannot exclude that a larger fraction of SNe Ic-BL harbors GRB 060218/SN 2006aj-like emission. In the future, obtaining fast and accurate spectral classifications of SNe Ic-BL paired with deep radio follow-up observations executed within 5 days since explosion would overcome this limitation. While high-cadence optical surveys can provide an alternative way to measure the rate of SNe Ic-BL that are similar to SN 2006aj via shock-cooling emission at early times, more optical detections are also needed to measure a robust rate.

The Legacy Survey of Space and Time (LSST) on the Vera C. Rubin Observatory (Ivezic et al. 2019) promises to provide numerous discoveries of even the rarest type of explosive transients, such as the SNe Ic-BL discussed here. The challenge will be to recognize and classify these explosions promptly (e.g., Villar et al. 2019, 2020), so that they can be followed up in the radio with current and next-generation radio facilities. Indeed, Rubin, paired with the increased sensitivity of the next-generation VLA (ngVLA; Selina et al. 2018), could provide a unique opportunity for building a large statistical sample of SNe Ic-BL with deep radio observations that may be used to guide theoretical modeling in a more systematic fashion, beyond what has been achievable over the last ≈ 25 yr (i.e.,

since the discovery of GRB-SN 1998bw). In addition, the Square Kilometer Array (SKA) will enable discoveries of radio SNe and other transients in an untargeted and optically unbiased way (Lien et al. 2011). These SKA discoveries would require relatively fast and multifrequency follow-up observations to be most impactful. Hence, overall, one can envision that the Rubin/LSST and SKA samples, enriched by ngVLA follow-up observations, will provide crucial information on massive star evolution, as well as SNe Ic-BL physics and CSM properties.

We conclude by noting that understanding the evolution of single and stripped binary stars up to core collapse is of special interest in the new era of time-domain multimessenger (gravitational wave and neutrino) astronomy (see, e.g., Scholberg 2012; Murase 2018; Abdikamalov et al. 2020; Guépin et al. 2022 for recent reviews). Gravitational waves from nearby core-collapse SNe, in particular, represent an exciting prospect for expanding multimessenger studies beyond the current realm of compact binary coalescences (e.g., Gottlieb et al. 2022). While they may come into reach with the current LIGO (The LIGO Scientific Collaboration 2015) and Virgo (Acernese et al. 2015) detectors, it is more likely that next-generation gravitational-wave observatories, such as the Einstein Telescope (Maggiore et al. 2020) and the Cosmic Explorer (Evans et al. 2021), will enable painting the first detailed multimessenger picture of a core-collapse explosion. The physics behind massive star evolution and death also impact the estimated rates and mass distribution of compact object mergers (e.g., Schneider et al. 2021), which, in turn, are current primary sources for LIGO and Virgo, and will be detected in much large numbers by next-generation gravitational-wave detectors. Hence, continued and coordinated efforts dedicated to understanding massive star deaths and the link between pre-SN progenitors and the properties of SN explosions, using multiple messengers, undoubtedly represent an exciting path forward.

Acknowledgments

A.C. and A.B. acknowledge support from NASA Swift Guest Investigator programs (Cycles 16 and 17 via grants #80NSSC20K1482 and #80NSSC22K0203). S.A. gratefully acknowledges support from the National Science Foundation GROWTH PIRE grant No. 1545949. S.Y. has been supported by the research project grant “Understanding the Dynamic Universe” funded by the Knut and Alice Wallenberg Foundation under Dnr KAW 2018.0067, and the G.R.E.A.T research environment, funded by *Vetenskapsrådet*, the Swedish Research Council, project number 2016–06012. Based on observations obtained with the Samuel Oschin Telescope 48-inch and the 60-inch Telescope at the Palomar Observatory as part of the Zwicky Transient Facility project. ZTF is supported by the National Science Foundation under grants Nos. AST-1440341 and AST-2034437, and a collaboration including Caltech, IPAC, the Weizmann Institute for Science, the Oskar Klein Center at Stockholm University, the University of Maryland, Deutsches Elektronen-Synchrotron and Humboldt University, Los Alamos National Laboratories, the TANGO Consortium of Taiwan, the University of Wisconsin at Milwaukee, Trinity College Dublin, Lawrence Berkeley National Laboratories, Lawrence Livermore National Laboratories, and IN2P3, France. Operations are conducted by COO, IPAC, and UW. The SED Machine is based upon work

supported by the National Science Foundation under grant No. 1106171. The ZTF forced-photometry service was funded under the Heising-Simons Foundation grant #12540303 (PI: Graham). The National Radio Astronomy Observatory is a facility of the National Science Foundation operated under cooperative agreement by Associated Universities, Inc. The Pan-STARRS1 Survey (PS1) and the PS1 public science archive have been made possible through contributions by the Institute for Astronomy, the University of Hawaii, the Pan-STARRS Project Office, the Max Planck Society and its participating institutes, the Max Planck Institute for Astronomy, Heidelberg and the Max Planck Institute for Extraterrestrial Physics, Garching, Johns Hopkins University, Durham University, the University of Edinburgh, the Queen’s University Belfast, the Harvard-Smithsonian Center for Astrophysics, the Las Cumbres Observatory Global Telescope Network Incorporated, the National Central University of Taiwan, the Space Telescope Science Institute, the National Aeronautics and Space Administration under grant No. NNX08AR22G issued through the Planetary Science Division of the NASA Science Mission Directorate, the National Science Foundation grant No. AST-1238877, the University of Maryland, Eotvos Lorand University (ELTE), the Los Alamos National Laboratory, and the Gordon and Betty Moore Foundation. Based in part on observations made with the Nordic Optical Telescope, owned in collaboration by the University of Turku and Aarhus University, and operated jointly by Aarhus University, the University of Turku and the University of Oslo, representing Denmark, Finland and Norway, the University of Iceland and Stockholm University at the Observatorio del Roque de los Muchachos, La Palma, Spain, of the Instituto de Astrofísica de Canarias.

Appendix A Sample Description

A.1. SN 2018etk

Our first ZTF photometry of SN 2018etk (ZTF18abklarx) was obtained on 2018 August 1 (MJD 58331.16) with the P48. This first ZTF detection was in the r band, with a host-subtracted magnitude of 19.21 ± 0.12 mag (Figure 1), at $\alpha = 15^{\text{h}}17^{\text{m}}02^{\text{s}}.53$, $\delta = +03^{\circ}56'38''.7$ (J2000). The object was reported to the TNS by ATLAS on 2018 August 8, who discovered it on 2018 August 6 (Tonry et al. 2018a). The last ZTF nondetection prior to ZTF discovery was on 2018 July 16, and the last shallow ATLAS nondetection was on 2018 August 2, at 18.75 mag. The transient was classified as a Type Ic SN by Fremling et al. (2018a) based on a spectrum obtained on 2018 August 13 with SEDM. We reclassify this transient as an SN Type Ic-BL most similar to SN 2006aj based on a P200 DBSP spectrum obtained on 2018 August 21 (see Figure 3). SN 2018etk exploded in a star-forming galaxy with a known redshift of $z = 0.044$ derived from SDSS data.

A.2. SN 2018hom

Our first ZTF photometry of SN 2018hom (ZTF18acbwxc) was obtained on 2018 November 1 (MJD 58423.54) with the P48. This first ZTF detection was in the r band, with a host-subtracted magnitude of 16.60 ± 0.04 mag (Figure 1), at $\alpha = 22^{\text{h}}59^{\text{m}}22^{\text{s}}.96$, $\delta = +08^{\circ}45'04''.6$ (J2000). The object was reported to the TNS by ATLAS on 2018 October 26, and discovered by ATLAS on 2018 October 24 at $o \approx 17.3$ mag

(Tonry et al. 2018b). The last ZTF nondetection prior to ZTF discovery was on 2018 October 9 at $g > 20.35$ mag, and the last ATLAS nondetection was on 2018 October 22 at $o > 18.25$ mag. The transient was classified as an SN Type Ic-BL by Fremling et al. (2018b) based on a spectrum obtained on 2018 November 2 with SEDM. SN 2018etk exploded in a galaxy with an unknown redshift. We measure a redshift of $z = 0.030$ from star-forming emission lines in a Keck I LRIS spectrum obtained on 2018 November 30. We plot this spectrum in Figure 3, along with its SNID template match to the Type Ic-BL SN 1997ef. We note that this SN was also reported in the recently released ASAS-SN bright SN catalog (Neumann et al. 2023).

A.3. SN 2018hxo

Our first ZTF photometry of SN 2018hxo (ZTF18acaimrb) was obtained on 2018 October 9 (MJD 58400.14) with the P48. This first detection was in the g band, with a host-subtracted magnitude of 18.89 ± 0.09 mag (Figure 1), at $\alpha = 21^{\text{h}}09^{\text{m}}05^{\text{s}}80$, $\delta = +14^{\circ}32'27''8$ (J2000). The object was first reported to the TNS by ATLAS on 2018 November 6, and first detected by ATLAS on 2018 September 25 at $o = 18.36$ mag (Tonry et al. 2018c). The last ZTF nondetection prior to discovery was on 2018 September 27 at $r > 20.12$ mag, and the last ATLAS nondetection was on 2018 September 24 at $o > 18.52$ mag. The transient was classified as an SN Type Ic-BL by Dahiwalé & Fremling (2020a) based on a spectrum obtained on 2018 December 1 with Keck I LRIS. In Figure 3 we plot this spectrum along with its SNID match to the Type Ic-BL SN 2002ap. SN 2018etk exploded in a galaxy with an unknown redshift. We measure a redshift of $z = 0.048$ from star-forming emission lines in the Keck spectrum.

A.4. SN 2018jex

Our first ZTF photometry of SN 2018jex (ZTF18acpeekw) was obtained on 2018 November 16 (MJD 58438.56) with the P48. This first detection was in the r band, with a host-subtracted magnitude of 20.07 ± 0.29 mag, at $\alpha = 11^{\text{h}}54^{\text{m}}13^{\text{s}}87$, $\delta = +20^{\circ}44'02''4$ (J2000). The object was reported to the TNS by AMPEL on November 28 (Nordin et al. 2018). The last ZTF last nondetection prior to ZTF discovery was on 2018 November 16 at $r > 19.85$ mag. The transient was classified as an SN Type Ic-BL based on a spectrum obtained on 2018 December 4 with Keck I LRIS. In Figure 3 we show this spectrum plotted against the SNID template of the Type Ic-BL SN 1997ef. AT2018jex exploded in a galaxy with an unknown redshift. We measure a redshift of $z = 0.094$ from star-forming emission lines in the Keck spectrum.

A.5. SN 2019hsx

We refer the reader to Anand et al. (2023) for details about this SN Ic-BL. Its P48 light curves and the spectrum used for classification are shown in Figures 1 and 3, respectively. We note that this SN was also reported in the recently released ASAS-SN bright SN catalog (Neumann et al. 2023).

A.6. SN 2019xcc

We refer the reader to Anand et al. (2023) for details about this SN Ic-BL. Its P48 light curves and the spectrum used for classification are shown in Figures 1 and 3, respectively.

A.7. SN 2020jqm

Our first ZTF photometry of SN 2020jqm (ZTF20aazkjfv) was obtained on 2020 May 11 (MJD 58980.27) with the P48. This first detection was in the r band, with a host-subtracted magnitude of 19.42 ± 0.13 mag, at $\alpha = 13^{\text{h}}49^{\text{m}}18^{\text{s}}57$, $\delta = -03^{\circ}46'10''4$ (J2000). The object was reported to the TNS by ALERCE on May 11 (Forster et al. 2020). The last ZTF nondetection prior to ZTF discovery was on 2020 May 08 at $g > 17.63$ mag. The transient was classified as an SN Type Ic-BL based on a spectrum obtained on 2020 May 26 with SEDM (Dahiwalé & Fremling 2020b). SN 2020jqm exploded in a galaxy with an unknown redshift. We measure a redshift of $z = 0.037$ from host-galaxy emission lines in a NOT ALFOSC spectrum obtained on 2020 June 6. We plot the ALFOSC spectrum along with its SNID match to the Type Ic-BL SN 1998bw in Figure 3.

A.8. SN 2020lao

We refer the reader to Anand et al. (2023) for details about this SN Ic-BL. Its P48 light curves and the spectrum used for classification are shown in Figures 1 and 3, respectively. We note that this SN was also reported in the recently released ASAS-SN bright SN catalog (Neumann et al. 2023).

A.9. SN 2020rph

We refer the reader to Anand et al. (2023) for details about this SN Ic-BL. Its P48 light curves and the spectrum used for classification are shown in Figures 1 and 4, respectively.

A.10. SN 2020tkx

We refer the reader to Anand et al. (2023) for details about this SN Ic-BL. Its P48 light curves and the spectrum used for classification are shown in Figures 1 and 4, respectively.

A.11. SN 2021xv

We refer the reader to Anand et al. (2023) for details about this SN Ic-BL. Its P48 light curves and the spectrum used for classification are shown in Figures 1 and 4, respectively.

A.12. SN 2021aug

Our first ZTF photometry of SN 2021aug (ZTF21aafnunh) was obtained on 2021 January 18 (MJD 59232.11) with the P48. This first detection was in the g band, with a host-subtracted magnitude of 18.73 ± 0.08 mag, at $\alpha = 01^{\text{h}}14^{\text{m}}04^{\text{s}}81$, $\delta = +19^{\circ}25'04''7$ (J2000). The last ZTF nondetection prior to ZTF discovery was on 2021 January 16 at $g > 20.12$ mag. The transient was publicly reported to the TNS by ALERCE on 2021 January 18 (Munoz-Arancibia et al. 2021a), and classified as an SN Type Ic-BL based on a spectrum obtained on 2021 February 09 with SEDM (Dahiwalé & Fremling 2021). SN 2020jqm exploded in a galaxy with an unknown redshift. We measure a redshift of $z = 0.041$ from star-forming emission lines in a P200 DBSP spectrum obtained

on 2021 February 08. This spectrum is shown in Figure 4 along with its template match to the Type Ic-BL SN 1997ef.

A.13. SN 2021epp

Our first ZTF photometry of SN 2021epp (ZTF21aaocrlm) was obtained on 2021 March 5 (MJD 59278.19) with the P48. This first ZTF detection was in the r band, with a host-subtracted magnitude of 19.61 ± 0.15 mag (Figure 1), at $\alpha = 08^{\text{h}}10^{\text{m}}55^{\text{s}}.27$, $\delta = -06^{\circ}02'49''$ 3 (J2000). The transient was publicly reported to the TNS by ALerCE on 2021 March 5 (Munoz-Arancibia et al. 2021b), and classified as an SN Type Ic-BL based on a spectrum obtained on 2021 March 13 by ePESSTO+ with the ESO Faint Object Spectrograph and Camera (Kankare et al. 2021). The last ZTF nondetection prior to discovery was on 2021 March 2 at $r > 19.72$ mag. In Figure 4 we show the classification spectrum plotted against the SNID template of the Type Ic-BL SN 2002ap. SN 2021epp exploded in a galaxy with a known redshift of $z = 0.038$.

A.14. SN 2021htb

Our first ZTF photometry of SN 2021htb (ZTF21aardvol) was obtained on 2021 March 31 (MJD 59304.164) with the P48. This first ZTF detection was in the r band, with a host-subtracted magnitude of 20.13 ± 0.21 mag (Figure 1), at $\alpha = 07^{\text{h}}45^{\text{m}}31^{\text{s}}.19$, $\delta = 46^{\circ}40'01''$ 4 (J2000). The transient was publicly reported to the TNS by SGLF on 2021 April 2 (Poidevin et al. 2021). The last ZTF nondetection prior to ZTF discovery was on 2021 March 2, at $r > 19.88$ mag. In Figure 4 we show a P200 DBSP spectrum taken on 2021 April 09 plotted against the SNID template of the Type Ic-BL SN 2002ap. SN 2021htb exploded in an SDSS galaxy with redshift $z = 0.035$.








A.15. SN 2021hyz

Our first ZTF photometry of SN 2021hyz (ZTF21aartgiv) was obtained on 2021 April 03 (MJD 59307.155) with the P48. This first ZTF detection was in the g band, with a host-subtracted magnitude of 20.29 ± 0.17 mag (Figure 1), at $\alpha = 09^{\text{h}}27^{\text{m}}36^{\text{s}}.51$, $\delta = 04^{\circ}27'11''$ (J2000). The transient was publicly reported to the TNS by ALerCE on 2021 April 3 (Forster et al. 2021). The last ZTF nondetection prior to ZTF discovery was on 2021 April 1, at $g > 19.15$ mag. In Figure 4 we show a P60 SEDM spectrum taken on 2021 April 30 plotted against the SNID template of the Type Ic-BL SN 1997ef. SN 2021hyz exploded in a galaxy with redshift $z = 0.046$.

A.16. SN 2021ywf

We refer the reader to Anand et al. (2023) for details about this SN Ic-BL. Its P48 light curves and the spectrum used for classification are shown in Figures 1 and 4, respectively.

ORCID iDs

Alessandra Corsi  <https://orcid.org/0000-0001-8104-3536>
 Anna Y. Q. Ho  <https://orcid.org/0000-0002-9017-3567>
 S. Bradley Cenko  <https://orcid.org/0000-0003-1673-970X>
 Shrinivas R. Kulkarni  <https://orcid.org/0000-0001-5390-8563>
 Shreya Anand  <https://orcid.org/0000-0003-3768-7515>
 Sheng Yang  <https://orcid.org/0000-0002-2898-6532>
 Jesper Sollerman  <https://orcid.org/0000-0003-1546-6615>

Gokul P. Srinivasaragavan  <https://orcid.org/0000-0002-6428-2700>
 Conor M. B. Omand  <https://orcid.org/0000-0002-9646-8710>
 Arvind Balasubramanian  <https://orcid.org/0000-0003-0477-7645>
 Christoffer Fremling  <https://orcid.org/0000-0002-4223-103X>
 Daniel A. Perley  <https://orcid.org/0000-0001-8472-1996>
 Yuhan Yao  <https://orcid.org/0000-0001-6747-8509>
 Kishalay De  <https://orcid.org/0000-0002-3961-1365>
 Matthew Hankins  <https://orcid.org/0000-0001-9315-8437>
 Jacob Jenson  <https://orcid.org/0000-0001-5754-4007>
 Mansi M. Kasliwal  <https://orcid.org/0000-0002-5619-4938>
 Anastasios Tzanidakis  <https://orcid.org/0000-0003-0484-3331>
 Eric C. Bellm  <https://orcid.org/0000-0001-8018-5348>
 Russ R. Laher  <https://orcid.org/0000-0003-2451-5482>
 Frank J. Masci  <https://orcid.org/0000-0002-8532-9395>
 Josiah N. Purdum  <https://orcid.org/0000-0003-1227-3738>

References

- Abdikamalov, E., Pagliaroli, G., & Radice, D. 2020, arXiv:2010.04356
 Acernese, F., Agathos, M., Agatsuma, K., et al. 2015, *CQGra*, 32, 024001
 Afsariardchi, N., Drout, M. R., Khatami, D. K., et al. 2021, *ApJ*, 918, 89
 Anand, S., Barnes, J., Yang, S., et al. 2023, arXiv:2302.09226
 Armstrong, M. 2002, IAU Circ., 7845, 1
 Arnett, W. D. 1982, *ApJ*, 253, 785
 Balasubramanian, A., Corsi, A., Polisensky, E., Clarke, T. E., & Kassim, N. E. 2021, *ApJ*, 923, 32
 Barnes, J., Duffell, P. C., Liu, Y., et al. 2018, *ApJ*, 860, 38
 Barthelmy, S. D., Barbier, L. M., Cummings, J. R., et al. 2005, *SSRv*, 120, 143
 Bazin, G., Palanque-Delabrouille, N., Rich, J., et al. 2009, *A&A*, 499, 653
 Becker, R. H., White, R. L., & Helfand, D. J. 1995, *ApJ*, 450, 559
 Bellm, E. C., Kulkarni, S. R., Graham, M. J., et al. 2019, *PASP*, 131, 018002
 Bennett, C. L., Larson, D., Weiland, J. L., & Hinshaw, G. 2014, *ApJ*, 794, 135
 Berger, E., Kulkarni, S. R., Frail, D. A., & Soderberg, A. M. 2003, *ApJ*, 599, 408
 Blagorodnova, N., Neill, J. D., Walters, R., et al. 2018, *PASP*, 130, 035003
 Blondin, S., & Tonry, J. L. 2007, *ApJ*, 666, 1024
 Bromberg, O., Nakar, E., & Piran, T. 2011, *ApJL*, 739, L55
 Bugli, M., Guilet, J., & Obergaulinger, M. 2021, *MNRAS*, 507, 443
 Bugli, M., Guilet, J., Obergaulinger, M., Cerdá-Durán, P., & Aloy, M. A. 2020, *MNRAS*, 492, 58
 Burrows, A., Dessart, L., Livne, E., Ott, C. D., & Murphy, J. 2007, *ApJ*, 664, 416
 Burrows, D. N., Hill, J. E., Nousek, J. A., et al. 2005, *SSRv*, 120, 165
 Campana, S., Mangano, V., Blustin, A. J., et al. 2006, *Natur*, 442, 1008
 Cano, Z., Wang, S.-Q., Dai, Z.-G., & Wu, X.-F. 2017, *AdAst*, 2017, 8929054
 Cardelli, J. A., Clayton, G. C., & Mathis, J. S. 1989, *ApJ*, 345, 245
 Chen, K.-J., Moriya, T. J., Woosley, S., et al. 2017, *ApJ*, 839, 85
 Chevalier, R. A. 1998, *ApJ*, 499, 810
 Chevalier, R. A., & Fransson, C. 2006, *ApJ*, 651, 381
 Corsi, A., Cenko, S. B., Kasliwal, M. M., et al. 2017, *ApJ*, 847, 54
 Corsi, A., Gal-Yam, A., Kulkarni, S. R., et al. 2016, *ApJ*, 830, 42
 Corsi, A., Ofek, E. O., Gal-Yam, A., et al. 2014, *ApJ*, 782, 42
 Dahiwal, A., & Fremling, C. 2020a, *TNSCR*, 2020-1924
 Dahiwal, A., & Fremling, C. 2020b, *TNSCR*, 2020-5921
 Dahiwal, A., & Fremling, C. 2021, *TNSCR*, 2021-405
 Dekany, R., Smith, R. M., Riddle, R., et al. 2020, *PASP*, 132, 038001
 Djupvik, A. A., & Andersen, J. 2010, in *Highlights of Spanish Astrophysics V*, Astrophysics and Space Science Proc. 14 (Berlin: Springer), 211
 Drake, A. J., Djorgovski, S. G., Mahabal, A., et al. 2009, *ApJ*, 696, 870
 Dark Energy Survey Collaboration, Abbott, T., Abdalla, F. B., et al. 2016, *MNRAS*, 460, 1270
 Eisenberg, M., Gottlieb, O., & Nakar, E. 2022, *MNRAS*, 517, 582
 Ellison, D. C., Berezhko, E. G., & Baring, M. G. 2000, *ApJ*, 540, 292
 Evans, M., Adhikari, R. X., Afle, C., et al. 2021, arXiv:2109.09882
 Evans, P. A., Beardmore, A. P., Page, K. L., et al. 2009, *MNRAS*, 397, 1177
 Filippenko, A. V. 1997, *ARA&A*, 35, 309
 Flewelling, H. A., Magnier, E. A., Chambers, K. C., et al. 2020, *ApJS*, 251, 7

- Foglizzo, T., Kazeroni, R., Guilet, J., et al. 2015, *PASA*, **32**, e009
- Forster, F., Bauer, F. E., Galbany, L., et al. 2020, *TNSTR*, **2020-1297**
- Forster, F., Bauer, F. E., Pignata, G., et al. 2021, *TNSTR*, **2021-1011**
- Fremming, C., Dugas, A., & Sharma, Y. 2018a, *TNSCR*, **2018-1169**
- Fremming, C., Dugas, A., & Sharma, Y. 2018b, *TNSCR*, **2018-1720**
- Frohmaier, C., Angus, C. R., Vincenzi, M., et al. 2021, *MNRAS*, **500**, 5142
- Galama, T. J., Vreeswijk, P. M., van Paradijs, J., et al. 1998, *Natur*, **395**, 670
- Gal-Yam, A., Ofek, E. O., & Shemmer, O. 2002, *MNRAS*, **332**, L73
- Gal-Yam, A. 2017, in *Handbook of Supernovae*, ed. A. Alsabti & P. Murdin (Cham: Springer), **195**
- Gehrels, N., Chincarini, G., Giommi, P., et al. 2004, *ApJ*, **611**, 1005
- Ghirlanda, G., & Salvaterra, R. 2022, *ApJ*, **932**, 10
- Gilkis, A., & Soker, N. 2014, *MNRAS*, **439**, 4011
- Gilkis, A., Soker, N., & Papish, O. 2016, *ApJ*, **826**, 178
- Gottlieb, O., Lalakos, A., Bromberg, O., Liska, M., & Tchekhovskoy, A. 2022, *MNRAS*, **510**, 4962
- Graham, M. J., Kulkarni, S. R., Bellm, E. C., et al. 2019, *PASP*, **131**, 078001
- Guépin, C., Kotera, K., & Oikonomou, F. 2022, *NatRP*, **4**, 697
- Heger, A., Fryer, C. L., Woosley, S. E., Langer, N., & Hartmann, D. H. 2003, *ApJ*, **591**, 288
- Ho, A. Y. Q., Corsi, A., Cenko, S. B., et al. 2020a, *ApJ*, **893**, 132
- Ho, A. Y. Q., Kulkarni, S. R., Perley, D. A., et al. 2020b, *ApJ*, **902**, 86
- Ho, A. Y. Q., Goldstein, D. A., Schulze, S., et al. 2019, *ApJ*, **887**, 169
- Iwamoto, K., Mazzali, P. A., Nomoto, K., et al. 1998, *Natur*, **395**, 672
- Izzard, R. G., Ramirez-Ruiz, E., & Tout, C. A. 2004, *MNRAS*, **348**, 1215
- Janka, H.-T. 2012, *ARNPS*, **62**, 407
- Janka, H. T., Langanke, K., Marek, A., Martínez-Pinedo, G., & Müller, B. 2007, *PhR*, **442**, 38
- Japelj, J., Vergani, S. D., Salvaterra, R., et al. 2018, *A&A*, **617**, A105
- Jerkstrand, A., Timmes, F. X., Magkotsios, G., et al. 2015, *ApJ*, **807**, 110
- Ivezić, Ž., Kahn, S. M., Tyson, J. A., et al. 2019, *ApJ*, **873**, 111
- Kaiser, N., Burgett, W., Chambers, K., et al. 2010, *Proc. SPIE*, **7733**, 77330E
- Kankare, E., Nagao, T., Koivisto, N., et al. 2021, *TNSCR*, **2021-762**
- Kelly, P. L., Filippenko, A. V., Modjaz, M., & Kocevski, D. 2014, *ApJ*, **789**, 23
- Kouveliotou, C., Woosley, S. E., Patel, S. K., et al. 2004, *ApJ*, **608**, 872
- Kulkarni, S. R., Frail, D. A., Wieringa, M. H., et al. 1998, *Natur*, **395**, 663
- Langer, N. 2012, *ARA&A*, **50**, 107
- Law, C. J., Gaensler, B. M., Metzger, B. D., Ofek, E. O., & Sironi, L. 2018, *ApJL*, **866**, L22
- Law, N. M., Kulkarni, S. R., Dekany, R. G., et al. 2009, *PASP*, **121**, 1395
- Lazzati, D., Morsony, B. J., Blackwell, C. H., & Begelman, M. C. 2012, *ApJ*, **750**, 68
- Li, W., Leaman, J., Chornock, R., et al. 2011, *MNRAS*, **412**, 1441
- Li, Z.-Y., & Chevalier, R. A. 1999, *ApJ*, **526**, 716
- Lien, A., Chakraborty, N., Fields, B. D., & Kembell, A. 2011, *ApJ*, **740**, 23
- Liu, Y.-Q., Modjaz, M., Bianco, F. B., & Graur, O. 2016, *ApJ*, **827**, 90
- Livio, M., & Waxman, E. 2000, *ApJ*, **538**, 187
- Lyman, J. D., Bersier, D., & James, P. A. 2014, *MNRAS*, **437**, 3848
- Lyman, J. D., Bersier, D., James, P. A., et al. 2016, *MNRAS*, **457**, 328
- MacFadyen, A. I., & Woosley, S. E. 1999, *ApJ*, **524**, 262
- Maeda, K., Chandra, P., Matsuoka, T., et al. 2021, *ApJ*, **918**, 34
- Maggiore, M., Van Den Broeck, C., Bartolo, N., et al. 2020, *JCAP*, **2020**, 050
- Margutti, R., Kamble, A., Milisavljevic, D., et al. 2017, *ApJ*, **835**, 140
- Margutti, R., Soderberg, A. M., Wieringa, M. H., et al. 2013, *ApJ*, **778**, 18
- Masci, F. J., Laher, R. R., Rusholme, B., et al. 2019, *PASP*, **131**, 018003
- Matheson, T., Filippenko, A. V., Li, W., Leonard, D. C., & Shields, J. C. 2001, *AJ*, **121**, 1648
- Mazzali, P. A., Deng, J., Maeda, K., et al. 2002, *ApJL*, **572**, L61
- Mazzali, P. A., Deng, J., Pian, E., et al. 2006a, *ApJ*, **645**, 1323
- Mazzali, P. A., Deng, J., Nomoto, K., et al. 2006b, *Natur*, **442**, 1018
- Mazzali, P. A., Deng, J., Tominaga, N., et al. 2003, *ApJL*, **599**, L95
- Mazzali, P. A., Iwamoto, K., & Nomoto, K. 2000, *ApJ*, **545**, 407
- Mazzali, P. A., MacFadyen, A. I., Woosley, S. E., Pian, E., & Tanaka, M. 2014, *MNRAS*, **443**, 67
- McMullin, J. P., Waters, B., Schiebel, D., Young, W., & Golap, K. 2007, in *ASP Conf. Ser. 376, Astronomical Data Analysis Software and Systems XVI*, ed. R. A. Shaw, F. Hill, & D. J. Bell (San Francisco, CA: ASP), **127**
- Meegan, C., Lichti, G., Bhat, P. N., et al. 2009, *ApJ*, **702**, 791
- Mészáros, P. 2006, *RPPH*, **69**, 2259
- Mezzacappa, A., Calder, A. C., Bruenn, S. W., et al. 1998, *ApJ*, **495**, 911
- Miller, A. A., Yao, Y., Bulla, M., et al. 2020, *ApJ*, **902**, 47
- Modjaz, M., Bianco, F. B., Siwek, M., et al. 2020, *ApJ*, **892**, 153
- Modjaz, M., Blondin, S., Kirshner, R. P., et al. 2014, *AJ*, **147**, 99
- Modjaz, M., Li, W., Butler, N., et al. 2009, *ApJ*, **702**, 226
- Modjaz, M., Liu, Y. Q., Bianco, F. B., & Graur, O. 2016, *ApJ*, **832**, 108
- Montes, M. J., Van Dyk, S. D., Weiler, K. W., Sramek, R. A., & Panagia, N. 1998, *ApJ*, **506**, 874
- Müller, B. 2020, *LRCA*, **6**, 3
- Munoz-Arancibia, A., Forster, F., Bauer, F. E., et al. 2021a, *TNSTR*, **2021-180**
- Munoz-Arancibia, A., Forster, F., Bauer, F. E., et al. 2021b, *TNSTR*, **2021-685**
- Murase, K. 2018, *PhRvD*, **97**, 081301
- Neumann, K. D., Holoien, T. W. S., Kochanek, C. S., et al. 2023, *MNRAS*, **520**, 4356
- Nishimura, N., Takiwaki, T., & Thielemann, F.-K. 2015, *ApJ*, **810**, 109
- Nordin, J., Brinnet, V., Giomi, M., et al. 2018, *TNSTR*, **2018-2043**
- Oke, J. B., Cohen, J. G., Carr, M., et al. 1995, *PASP*, **107**, 375
- Oke, J. B., & Gunn, J. E. 1982, *PASP*, **94**, 586
- Pais, M., Piran, T., & Nakar, E. 2023, *MNRAS*, **519**, 1941
- Palliyaguru, N. T., Corsi, A., Frail, D. A., et al. 2019, *ApJ*, **872**, 201
- Papish, O., & Soker, N. 2011, *MNRAS*, **416**, 1697
- Perley, D. A., Fremming, C., Sollerman, J., et al. 2020, *ApJ*, **904**, 35
- Pian, E., Mazzali, P. A., Masetti, N., et al. 2006, *Natur*, **442**, 1011
- Piran, T. 2004, *RvMP*, **76**, 1143
- Piran, T., Nakar, E., Mazzali, P., & Pian, E. 2019, *ApJL*, **871**, L25
- Poidevin, F., Perez-Fourmon, L., Angel, C. J., et al. 2021, *TNSTR*, **2021-1003**
- Rigault, M., Neill, J. D., Blagorodnova, N., et al. 2019, *A&A*, **627**, A115
- Salas, P., Bauer, F. E., Stockdale, C., & Prieto, J. L. 2013, *MNRAS*, **428**, 1207
- Sand, D., Valenti, S., Tartaglia, L., Yang, S., & Wyatt, S. 2018, AAS Meeting, **231**, 245.11
- Sauer, D. N., Mazzali, P. A., Deng, J., et al. 2006, *MNRAS*, **369**, 1939
- Schlaflly, E. F., & Finkbeiner, D. P. 2011, *ApJ*, **737**, 103
- Schneider, F. R. N., Podsiadlowski, P., & Müller, B. 2021, *A&A*, **645**, A5
- Scholberg, K. 2012, *ARNPS*, **62**, 81
- Schulze, S., Klose, S., Björnsson, G., et al. 2011, *A&A*, **526**, A23
- Selina, R. J., Murphy, E. J., McKinnon, M., et al. 2018, in *ASP Conf. Ser. 517, Science with a Next Generation Very Large Array*, ed. E. Murphy (San Francisco, CA: ASP), **15**
- Shankar, S., Mösta, P., Barnes, J., Duffell, P. C., & Kasen, D. 2021, *MNRAS*, **508**, 5390
- Shappee, B. J., Prieto, J. L., Grupe, D., et al. 2014, *ApJ*, **788**, 48
- Shivvers, I., Modjaz, M., Zheng, W., et al. 2017, *PASP*, **129**, 054201
- Smith, N. 2014, *ARA&A*, **52**, 487
- Smith, N., Li, W., Filippenko, A. V., & Chornock, R. 2011, *MNRAS*, **412**, 1522
- Soderberg, A. M., Chakraborti, S., Pignata, G., et al. 2010, *Natur*, **463**, 513
- Soderberg, A. M., Chevalier, R. A., Kulkarni, S. R., & Frail, D. A. 2006a, *ApJ*, **651**, 1005
- Soderberg, A. M., Nakar, E., Berger, E., & Kulkarni, S. R. 2006b, *ApJ*, **638**, 930
- Soderberg, A. M., Kulkarni, S. R., Berger, E., et al. 2004, *Natur*, **430**, 648
- Soker, N., & Gilkis, A. 2017, *ApJ*, **851**, 95
- Stroh, M. C., Terreran, G., Coppejans, D. L., et al. 2021, *ApJL*, **923**, L24
- Suwa, Y., & Tominaga, N. 2015, *MNRAS*, **451**, 282
- Taddia, F., Sollerman, J., Fremming, C., et al. 2019, *A&A*, **621**, A71
- The LIGO Scientific Collaboration 2015, *CQGra*, **32**, 074001
- Tonry, J., Stalder, B., Denneau, L., et al. 2018a, *TNSTR*, **2018-1123**
- Tonry, J., Denneau, L., Heinze, A., et al. 2018b, *TNSTR*, **2018-1634**
- Tonry, J., Denneau, L., Heinze, A., et al. 2018c, *TNSTR*, **2018-1713**
- Tonry, J. L., Denneau, L., Heinze, A. N., et al. 2018d, *PASP*, **130**, 064505
- Valenti, S., Benetti, S., Cappellaro, E., et al. 2008, *MNRAS*, **383**, 1485
- van Eerten, H., van der Horst, A., & MacFadyen, A. 2012, *ApJ*, **749**, 44
- van Eerten, H. J., & MacFadyen, A. I. 2011, *ApJL*, **733**, L37
- Villar, V. A., Berger, E., Miller, G., et al. 2019, *ApJ*, **884**, 83
- Villar, V. A., Hosseinzadeh, G., Berger, E., et al. 2020, *ApJ*, **905**, 94
- Villareal Hernández, A. C., & Andernach, H. 2018, arXiv:1808.07178
- Waxman, E. 2004, *ApJ*, **602**, 886
- Willingale, R., Starling, R. L. C., Beardmore, A. P., Tanvir, N. R., & O'Brien, P. T. 2013, *MNRAS*, **431**, 394
- Woosley, S. E., & Bloom, J. S. 2006, *ARA&A*, **44**, 507
- Woosley, S. E., & Heger, A. 2006, *ApJ*, **637**, 914
- Woosley, S. E., Heger, A., & Weaver, T. A. 2002, *RvMP*, **74**, 1015
- Yao, Y., Miller, A. A., Kulkarni, S. R., et al. 2019, *ApJ*, **886**, 152
- Yaron, O., & Gal-Yam, A. 2012, *PASP*, **124**, 668
- York, D. G., Adelman, J., Anderson, J. E. J., et al. 2000, *AJ*, **120**, 1579
- Young, T. R. 2004, *ApJ*, **617**, 1233
- Zhang, W., & MacFadyen, A. 2009, *ApJ*, **698**, 1261